Theses and Dissertations 1. Thesis and Dissertation Collection, all items

2002-12

Experimental Investigation into the Effects of Riblets on Compressor Cascade Performance.

Rothenflue, James A.

http://hdl.handle.net/10945/10804

AD-A243 881

DTIC
S ELECTE
JAN 0 6 1992
D D

EXPERIMENTAL INVESTIGATION INTO THE
EFFECTS OF RIBLETS ON COMPRESSOR
CASCADE PERFORMANCE

THESIS

JAMES A. POTHENFLUE

AFIT/GAE/ENY/91D-5

92-00042

20000901053

AFIT/GAE/ENY/91D-5

EXPERIMENTAL INVESTIGATION INTO THE EFFECTS OF RIBLETS ON

COMPRESSOR CASCADE PERFORMANCE

THESIS

Presented to the Faculty of the School of Engineering

of the Air Force Institute of Technology

Air University

In Partial Fulfillment of the

Requirements for the Degree of

Master of Science in Aeronautical Engineering

JAMES A. ROTHENFLUE

December 1991

Approved for public release: distribution unlimited.

Acknowledgements

The successful completion of an experimental project such as this one is never possible without the contributions of many individuals. This is especially true in the case of this thesis. I would like to express my sincere thanks to my advisor, Dr. William Elrod, for his indispensable guidance during all phases of this project, from conception to completion. I would also like to thank the members of my thesis committee, Dr. Paul King and Dr. Milton Franke for their advice which kept me on track. The experimental work for this thesis would have never been completed were it not for the tireless efforts of Steve DeCook, who guided me through the maze of Tygon tubing and electrical circuitry that is the AFIT "shark tank." Considerable thanks go to the AFIT lab technicians Mr. Jay Anderson, Mr. Dan Rioux, Mr. Mark Derriso, and especially Mr. Andy Pitts, whose bloodied knuckles will forever serve as an inspiration to this researcher. Mr. Nick Yardich, the laboratory supervisor, was always willing to provide that extra "push" that is sometimes necessary in the military procurement cycle. Mr. John Brohas and the rest of the AFIT model shop personnel deserve considerable recognition as well for their invaluable support and rapid turn-around times.

Finally, I save my sincerest gratitude for my wife, Lisa, who has _always_ been willing to drop whatever she's

doing to give me a hand. Without her constant support, this project would have never been completed.

James Andrew Rothenflue

iii

Table of Contents

List of Figures

List of Tables

List of Symbols

Symbol

AFIT	Air Force Institute of Technology
AVDR	axial velocity density ratio
CTF	Cascade Test Facility

Arabic Symbols

a	maximum camber location in fraction of chord length
A	surface area, film calibration equation coefficient
AR	aspect ratio
b	temperature loading factor exponent, bisector
B	coefficient of film calibration equation
c	chord length (ft)
C	coefficient of film calibration equation
c_f	local skin friction coefficient
C_p	static pressure rise coefficient
d_s	diameter of sensing element (ft)
h	riblet height from peak to valley (ft)
h^+	non-dimensional riblet height
h_f	convection coefficient of fluid
hp	horsepower
i	incidence angle (deg)
I_s	current through sensor (Amps)
l_s	length of sensing element (ft)
k	cooling ratio
k_1	cooling ratio for sensor #1
k_2	cooling ratio for sensor #2
k_f	fluid conductive heat transfer coefficient
k_o	reference fluid conductive heat transfer coefficient
Nu	Nusselt number
p	static pressure (lbf/ft^2)
p_1	upstream static pressure (lbf/ft^2)

P_2	downstream static pressure (lbf/ft^2)
P_o	total pressure (lbf/ft^2)
PLC	total pressure loss coefficient
psi	pounds force per square inch
q	dynamic pressure (lbf/ft^2)
q_1	inlet dynamic pressure (lbf/ft^2)
r_c	adiabatic wall recovery factor
R_3	upper arm voltage = R_u (volts)
R_c	cable resistance (ohms)
R_{pi}	internal probe resistance (ohms)
R_{ps}	probe support resistance (ohms)
R_s	resistance of sensor (ohms)
R_u	upper arm voltage (volts)
R_w	resistance of wire (ohms)
Re	Reynolds number
Re_c	blade chord Reynolds number
Re_x	local Reynolds number
s	riblet spacing, blade spacing (ft)
s^+	riblet non-dimensional spacing
T_f	temperature of fluid ($^\circ F$)
T_o	total (stagnation) temperature ($^\circ F$)
T_r	reference temperature ($^\circ F$)
T_s	temperature of sensor ($^\circ F$)
Tu	turbulence level (percent)
U_{FS}	free stream velocity (ft/sec)
V	velocity (ft/sec)
V_b	bridge voltage (volts)
V_s	voltage across sensor (volts)
x	axial direction (ft)
y	pitch direction, vertical distance from surface (ft)
y^+	non-dimensional vertical distance from surface

z	span direction (ft)

Greek Symbols

α	angle between wire and velocity vector
α_1	flow inlet angle, flow angle wrt sensor #1
α_1'	blade inlet angle
α_2	flow exit angle, flow angle wrt sensor #2
α_2'	blade outlet angle with respect to axial
β	flow angle wrt to probe axis
δ	deviation angle
θ	airfoil camber angle
μ	fluid viscosity
μ_0	reference fluid viscosity
ν	kinematic viscosity
ρ	air density
ρ_2	exit air density
ϖ	mass averaged total pressure loss coefficient
σ	cascade solidity = c/s
χ	stagger angle

Velocity Subscripts

1	upstream, relative to sensor 1
2	downstream, relative to sensor 2
eff	effective
in	inlet
p	perpendicular to sensor
rms	root mean square
x	component in axial direction
y	component in pitch direction

Abstract

The effects of adding riblets to the blades of a
subsonic, linear compressor cascade were investigated at
the Air Force Institute of Technology. Three blade config-
urations were tested, including a set of unmodified NACA
64-A905 series blades, a set with riblets applied to the
suction surface, and a set with riblets on the pressure
surface. Performance was evaluated over a wide range of
Reynolds numbers, and at low and high free stream turbu-
lence levels. Cascade performance was evaluated in terms
of total pressure loss coefficient, turning angle, and
static pressure rise. No riblet configuration offered
robust cascade performance improvements; however, perfor-
mance was significantly enhanced under certain specific
conditions. Riblets also degraded cascade performance at
other conditions.

EXPERIMENTAL INVESTIGATION INTO THE EFFECTS OF RIBLETS ON COMPRESSOR CASCADE PERFORMANCE

I. Introduction

Scope

Advanced airbreathing engine technology is critical to the maintenance United States military superiority. In addition, the American aerospace industry's dominance of worldwide markets has recently been challenged by foreign competitors. Continued technological superiority in the area of airbreathing propulsion is critical to American competitiveness in this market.

One measure of this superiority is the efficiency at which the compressor in a turbojet or turbofan engine performs its role. The basic turbojet cycle can be broken down into three parts: compression of the inlet air via the compressor, heat addition to the inlet air via the combustor, and expansion of the gasses through the turbine and exhaust nozzle. The power to drive the compressor is taken directly from the exhaust via the turbine. If the power requirements of the compressor can be reduced by increasing its efficiency, less power need be extracted by the turbine and more is available for the nozzle. The engine will therefore be able to deliver more thrust for a given amount of heat addition. Alternately, since the

1

means for heat addition to the cycle air of a turbojet engine is the combustion of fuel, less fuel need be burned to deliver a given thrust.

Most modern turbojet and turbofan engines use axial flow compressors. These compressors rely on a series of "stages" to compress the air flowing through them. Each stage consists of a rotating set of blades followed by a stationary set. Each of these blade rows is designed to turn the air which is flowing through it, and in so doing, increase its static pressure. The efficiency at which these blade rows turn the air is directly related to the maximum achievable pressure rise through the stage. If the pressure rise through each stage can be increased, fewer stages will be required in order to achieve a desired overall pressure ratio. Therefore, increased compressor efficiency leads to lighter engines, increased thrust-to-weight ratios, and improved economy.

This thesis documents an experimental investigation into one proposed avenue through which the blading within such a compressor may be improved. Small grooves, or "riblets", may be cut into the surface of the blades to increase their efficiency. Riblets have been shown to reduce the skin friction drag over a surface which is immersed in a turbulent boundary layer (18). Since skin friction drag is a significant contributor to the losses in an axial flow compressor, riblets may represent a means by

2

which these losses can be reduced.

The simplest way to simulate the flow within an axial compressor is through the use of a linear compressor cascade. Such cascades consist of a long row of identical blades and can simulate the most important flow conditions that would be seen by a similar set of blades within a rotating machine. Since cascades cannot exactly duplicate the extremely complicated flow conditions within a real compressor, useful cascade experimentation is often limited to an ideal case termed "two-dimensional". Two-dimensionality refers to a condition in which the cascade simulates an infinitely long row of blades that have an infinite span. The flow within such a cascade would have no velocity components in a direction parallel to the blade span; therefore, any streamline in the flow will be confined to a flat, two-dimensional plane.

Objective

This investigation had three goals. The first goal was to determine whether the riblets had any measurable effect on the performance of the cascade. If so, the second goal was to establish each set flow conditions under which the riblets' effects were noted. Finally, the third goal was to estimate the magnitude of these effects and determine whether the riblets benefitted or degraded cascade performance. Several criteria were used to gauge this performance, including total pressure loss, flow

turning angle, static pressure rise, and the shape of the
wake velocity profile behind a representative cascade
blade.

II.   Theory

Potential Theory for Cascades

Coordinate System. Before beginning the theoretical
discussion, it is necessary to define the linear cascade
coordinate system that is used in this thesis. This system
is illustrated in Figure 1. The x, or "axial", coordinate
is perpendicular to the cascade row and points downstream
of the cascade trailing edge. The y, or "pitch", coordi-
nate is parallel to the cascade row and points in the
direction in which the flow is turned by the cascade.
Finally, the z, or span, coordinate is parallel to the
trailing edge of the blades, pointing in a direction that
is consistent with a right handed coordinate system. The
origin of this coordinate system is at the center span
point of the trailing edge of the center blade of the
cascade. More details regarding the geometry of a linear
cascade and its coordinate system are given in Chapter III,
Apparatus.

Potential Theory. The analysis of the flow through a
linear cascade is greatly simplified by the assumptions of
inviscid and incompressible flow. The basic aerodynamic
function of a compressor cascade is to transform a portion
of the kinetic energy within a flow into potential energy.
The flow entering the cascade has a significant velocity

component in the negative pitchwise direction. If the cascade turns the incoming air directly to the axial direction and no change in the axial component of velocity takes place, the cascade will transform the kinetic energy associated with the pitchwise velocity component into a static pressure increase by diffusion. Given these assumptions, the rise in static pressure along a streamline in an incompressible fluid can be derived from Bernoulli's equation to equal

$$\Delta p = p_2 - p_1 = \frac{1}{2} \rho V_y^2 \tag{1}$$

where V_y represents the pitchwise velocity component of the incoming flow.

For the more common case of a cascade turning the flow to a direction other than the axial, the following relationships express the pressure rise through the cascade in terms of the inlet and outlet velocities, or the inlet velocity and the flow turning angles (7; 13-15):

$$\Delta p = \frac{1}{2} \rho (V_1^2 - V_2^2) = \frac{1}{2} \rho V_1^2 \left(1 - \frac{\cos^2 \alpha_1}{\cos^2 \alpha_2}\right). \tag{2}$$

Here, α_1 and α_2 are the flow inlet and outlet angles, to be formally defined later. This pressure rise represents a theoretical maximum which, in reality, cannot be achieved due to the dissipative action of viscosity in the fluid.

6

An overview of potential theory for cascades, including the derivation of Equation (2), is given in Appendix E.

Measures of Cascade Performance

In reality, viscosity plays a significant role in determining the nature of cascade flow. Since a viscous fluid cannot slip along a solid surface, a "boundary layer" of low speed flow develops near the surface where the influence of viscosity is non-negligible. The thickness of the boundary layer is normally defined as the depth of that region near the surface where the flow velocity is less than 99.5 percent of the freestream velocity. This loss in flow velocity within the boundary layer creates a non-recoverable momentum deficit, and, therefore, a loss in the average total pressure of the flow.

The interaction of the boundary layer with the externally imposed pressure gradients from the potential flow-field is an important consideration. An adverse pressure gradient exists over the majority of the suction surface of an axial compressor blade. This gradient will decelerate the flow over that portion of the blade's surface. If in addition to the pressure imposed deceleration, the fluid within the boundary layer is losing momentum to viscous dissipation, a point will be reached near the surface of the airfoil where backflow develops. This is called the separation point. Under normal operating conditions, this

7

region of separated flow is restricted to the extreme downstream end of the blade, near the trailing edge.

At the trailing edge of each airfoil in the cascade, this separated region from the suction surface coalesces with the pressure surface boundary layer to form a wake. This is illustrated in Figure 2. As the wake propagates downstream, it is re-energized by the surrounding flow, but at the expense free stream momentum. As this re-energization takes place, viscous dissipation continues within the flow due to the presence of velocity gradients and turbulence. Studies have shown that approximately 90 percent of the loss in total pressure downstream of the cascade due to wake induced viscous dissipation occurs within the first half chord length behind the blade (11:13).

The losses which occur within and downstream of a cascade are commonly expressed in terms of the total pressure loss coefficient, which is given by (14:201):

$$\tilde{\omega} = \frac{\Delta \tilde{P}_o}{\frac{1}{2}\rho_1 V_1^2} .$$

(3)

$\Delta \tilde{P}_o$ = mass-averaged cascade total pressure loss

The mass averaged value for any quantity, "A" for example, is given by:

$$\tilde{A} = \frac{\int\limits_{-s/2}^{s/2} \int\limits_{-z/2}^{z/2} \rho_2 V_{x_2} A\, dz\, dy}{\int\limits_{-s/2}^{s/2} \int\limits_{-z/2}^{z/2} \rho_2 V_{x_2}\, dz\, dy} \qquad\qquad (4)$$

where s equals one blade spacing and z is the span over which the data is averaged. So, in the case of the above definition for total pressure loss coefficient, $A = (P_{o1} - P_{o2})$. In other words, A is the measured difference between the total pressure upstream of the cascade and the total pressure at any given point downstream.

The analysis of blade wake velocity profiles in this thesis is primarily qualitative in nature. Although a variety of parameters exist with which the shape and size of a velocity profile can be described, the primary purpose of these parameters is to allow the comparison of one profile with another. For the purposes of this investigation, graphical comparisons of the important profiles sufficed. The mass averaged total pressure loss coefficient, turning angle, and the static pressure rise across the cascade were the parameters used for quantification of cascade performance.

Cascade Two-Dimensionality

As previously mentioned, two dimensionality refers to a flow condition in which each streamline in the flow is confined to a plane in space. For cascade flow, this plane

9

is the $x - y$ plane. The influence of any velocity components in the z direction should be zero, or, at least negligible.

Unfortunately, without considerable control measures, the flow within a low aspect ratio linear compressor cascade will be strongly three dimensional (7). The aspect ratio of a cascade is defined as the span of its blades divided by the chord. This three dimensional flow is due primarily to the development of a large vortex where each cascade blade's suction surface intersects a sidewall of the test section. The location of such a vortex is illustrated in Figure 3, and two such vortices will be generated by each blade in the cascade. These vortices are produced by the interaction of the pitchwise static pressure gradient between adjacent cascade blades and the low momentum fluid within the sidewall boundary layer. The details of corner wall vortex generation are given in Gostelow (7). For this discussion, it is sufficient to note that the removal of the sidewall boundary layer will inhibit corner wall vortex development. In cascades with aspect ratios greater than approximately four to five, the corner wall vortices are confined to a relatively small region near the sidewalls. Therefore, their influence on the flow over the centerline of the blades is small. However, on lower aspect ratio cascades, these vortices will strongly influence the flow over the entire suction surface of the blades

10

if allowed to develop freely.

To inhibit the development of these vortices, boundary layer removal must be employed on the test section sidewalls. The two most common methods for removing this boundary layer are upstream sidewall suction slots and porous sidewalls (7). Suction slots are effective in removing the upstream boundary layer ahead of the cascade, but they do nothing to prevent the development of a new boundary layer within the cascade. On the other hand, porous sidewalls are excellent at preventing the growth of the boundary layer within the cascade; however, they are less effective at removing the upstream boundary layer. Porous sidewalls were chosen for use in this investigation.

The degree of two-dimensionality of the flow within a linear cascade can be expressed in terms of the axial velocity density ratio (AVDR), defined by

$$AVDR = \frac{\int\limits_{-s/2}^{s/2} (\rho_2 V_{x_2})_{midspan}\, dy}{\int\limits_{-s/2}^{s/2} (\rho_1 V_{x_1})_{midspan}\, dy}. \tag{5}$$

The velocity and density values used for this calculation should be measured immediately upstream of the cascade and immediately downstream of the cascade. For a perfectly two-dimensional flow, the AVDR will equal one. If the flow through the centerline of the cascade ($z = 0$) is being

11

accelerated due to three dimensional effects, the *AVDR* will increase. For situations where the centerline flow is being decelerated, the *AVDR* will decrease. According to Scholz (16:489), an AVDR of 0.8 to 1.2 is sufficient for the assumption of quasi two-dimensional flow at the midspan of the cascade.

Riblet Theory

A universally accepted theory which describes the interaction of riblets with boundary layers does not yet exist. However, considerable experimental evidence regarding the effects of riblets on viscous drag is available (3, 18, 19). The drag reducing effects of adding riblets to a surface are primarily restricted to situations in which the boundary layer is turbulent. Laminar boundary layers are largely unaffected by small scale surface irregularities, unless those irregularities are large enough to initiate transition.

M. J. Walsh (18) identified an optimal riblet height and spacing for viscous drag reduction over a flat plate in low speed flows. His conclusions were that riblets with a non-dimensional height of approximately 10 and a non dimensional spacing of approximately 15 maximized viscous drag reduction (18:485-486). The non-dimensional height and spacing, h^+ and s^+ respectively, are defined as follows:

$$h^{+} = \sqrt{\frac{c_f}{2}} \left(\frac{h U_{FS}}{v} \right); \qquad s^{+} = \sqrt{\frac{c_f}{2}} \left(\frac{s U_{FS}}{v} \right) \qquad (6)$$

where

c_f = local skin friction coefficient,

U_{FS} = free stream velocity,

s = peak to peak spacing of riblets,

h = valley to peak height of riblets, and

v = kinematic viscosity of fluid.

At the optimum size, the riblets reduced skin friction drag over the surface by 8 percent. Similar results were presented by Bacher and Smith (3:1382-1384). In addition, riblets as large as $h^{+} = 25$ to 30 were shown to reduce viscous drag, as were riblets as small as $h^{+} = 5$. Also noted in these studies was that, for $h^{+} > 30$, the riblets increased the viscous drag due to the increased wetted area of the surface. For $h^{+} < 5$, no change in drag was noted.

The above optimum riblet sizes for drag reduction coincide closely with the laminar sublayer thickness within a turbulent boundary layer. The laminar sublayer is that region of flow in the immediate vicinity of the wall where the high turbulence which is predominant throughout the rest of the boundary layer is replaced by an essentially laminar flow. The commonly used equation for the estimation of the laminar sublayer thickness in a turbulent boundary layer is

13

$$y = \frac{y^+ v}{U_{FS}} \sqrt{\frac{2}{c_f}} ,$$

(7)

where $y^+ = 10$ (18:401). For a hydraulically smooth and flat surface, an empirical relationship for the turbulent c_f is as follows (15:639):

$$c_f = 0.0592 (Re_x)^{-0.2}.$$

(8)

These relationships can be used to arrive at a 1st order approximation of laminar sublayer thickness, even for a moderately curved surface.

Riblets have also been shown to affect the flow in diffusers and around free bodies. Martens (12) showed that separation in a straight walled diffuser can be delayed dramatically by the addition of riblets to the diffuser walls. Reagan (13) demonstrated similar results regarding pressure recovery in a such a diffuser. The effects of riblets on the flow around a cylinder and airfoil were investigated by Wieck (20). His results, although less dramatic, indicate that riblets are effective in delaying flow separation over these bodies. Since a compressor cascade combines elements of both diffusers and airfoils, it is reasonable to expect some improvement in performance due to the addition of riblets to the blades' surfaces.

III.   Apparatus

The Cascade Test Facility

The facility used for this investigation was the AFIT
Cascade Test Facility (CTF), located in Building 640, Area
B, Wright Patterson AFB, Ohio. A sketch of the CTF is
given in Figure 4, and the details of its general design
can be found in the thesis by Allison (2). The CTF has
undergone many changes since Allison's work was published,
and those modifications which are relevant to this study
will be discussed in detail in the following paragraphs.
In addition, individual component specifications and serial
numbers are listed in Appendix A.

General Layout

As illustrated in Figure 4, the output from the CTF's
air supply system was constricted through a 5 inch diameter
duct, and then diffused into a 44 inch diameter stilling
chamber. The stilling chamber contained a set of 40 mesh
wire screens, a felt filter, and a 4 inch honeycomb grid.
An adjustable ASME standard long radius bell mouth nozzle
then directed the flow into the test section. The entrance
to the test section was 2.0 inches in width and 6.9 inches
in height.

Air Supply System

For this investigation, the CTF air supply system was
modified to allow the controlled delivery of air over a

15

wide range of test section Reynolds numbers. The system consisted of two components: a 40 hp blower, and a 100 psi compressed air ejector.

Blower. The 40 hp centrifugal blower had a nameplate rating of 3000 ft^3/min at 26 ounces of head (2:3). The blower operated at one speed only and provided approximately 3.2 lbm/sec of air to the test section at a total head of approximately 1.5 psi. This resulted in a test section Reynolds number of approximately $1.8 \cdot 10^6$ ft^{-1}.

Ejector. The CTF ejector was installed immediately downstream of the blower housing and its geometry remains unchanged from the description given in Allison's thesis (2). It utilized a single converging-diverging nozzle with an 0.75 inch throat diameter.

The ejector's compressed air supply was the AFIT laboratory air, which was nominally maintained at 100 psi. This air was provided by two high capacity compressors which were operated either singly or in parallel. If only one compressor was operating, the maximum flow capability of the ejector to the test section was 0.6 psi total head and just over 2 lbm/sec of flow delivered to the test section. If both compressors were operating, the maximum total head increased to about 1.2 psi. In addition to operating at full power, the ejector was throttled in order to allow testing at a variety of test section Reynolds numbers. Therefore, using the ejector, the test section

Reynolds number could be set anywhere from zero to approximately $1.5 \cdot 10^6$ ft^{-1}.

The primary difficulty encountered in throttling the CTF ejector was in maintaining a steady air flow to the test section for the entire duration of a test. This required that the delivery pressure to the ejector be tightly controlled. This control was achieved by the installation of a Grove PowReactor dome valve and a bypass air gate valve into the ejector air supply assembly. The dome valve was used to adjust the mass flow through the CTF to near the desired value. The bypass valve was then used vent as much air as necessary to bring the pressure in the laboratory air system down to a level where the AFIT compressors were operating full time. Finally, fine adjustments to the dome valve setting were made in order to set the desired test section Reynolds number. Dome valve adjustments were performed by changing its reference pressure via a Grove reducing and relief regulator. When set properly, this system insulated the CTF from any pressure fluctuations in the AFIT laboratory air supply. A schematic of the CTF ejector pressure regulation system is given in Figure 5.

Test Section

The test section used for this investigation was composed of three components: the turbulence injector, the cascade region, and the exit. The entire test section is

illustrated in Figure 6. The turbulence injector and the cascade region were modified for this investigation while the exit remained unchanged. Each component will now be described separately.

Turbulence Injector. The turbulence level of the CTF air flow was elevated for some tests by injecting high pressure air from the test section sidewalls immediately upstream of the cascade region. Seven equally spaced, 1/16 inch diameter holes were drilled into each sidewall of the turbulence injector for this purpose. The injector holes were in a straight line that was approximately parallel with the cascade row. As illustrated in Figure 7, this arrangement provided a uniform turbulence level along the entire length of the cascade. The 100 psi laboratory air was the compressed air supply for the turbulence injector.

Cascade Region. The linear cascade used for this investigation had seven blades, with the outermost blades imbedded in the endwalls. Since the geometry of a linear cascade is closely related to the geometry of the airfoils of which it is composed, this description of the cascade will begin with a description of its blades.

Figure 8 illustrates the conventions used in this document regarding the geometrical description of an airfoil. An airfoil is defined by its camber line and its thickness distribution about that line. The thickness is normally measured perpendicularly to the chord line. The

chord line is the straight line that connects the leading
and trailing ends of the camber line. Its length, called
the chord, is designated by the symbol c. Finally, the
camber, given by θ, is the angle between the tangents to
the camber line at the trailing and leading edges.

Figure 9 illustrates the important cascade geometry
variables (7:7). As discussed in Chapter II, the axes of
the cascade coordinate system are defined by the axial,
pitch, and span directions. The angle between the inlet
velocity vector and the axial direction was 31°. The other
important cascade variables are given in Table 1, and are
described as follows. The stagger angle (χ) is the angle
between the blade's chord line and the axial. The spacing
(s) is the distance between the leading edges of any two
adjacent blades in the cascade, and the cascade's solidity
(σ) is defined by the ratio, c/s. Several other angles are
defined on Figure 9 that relate the orientation of the
flow's inlet and outlet velocity vectors to the cascade's
geometry. The deviation angle of the exit flow, δ, and the
flow exit angle, ω_2', differed for each test case during
this investigation.

The shape of the blades approximated that of a NACA
64-A905 (a = 0.5) series airfoil. This profile, due to its
large camber angle, is characteristic of the final stator
row in an axial flow compressor. The details regarding the
camber line and thickness distribution of this airfoil are

19

given in Appendix F.

Table 1.   Cascade Geometry

Characteristic	Symbol	Value
Blade chord	c	2.0 in
Aspect ratio	AR	1.0
Blade spacing	s	1.33 in
Blade camber	c	34.08°
Cascade solidity	σ	1.5
Stagger angle	χ	7.75°
Flow inlet angle	α_1	31.0°
Blade inlet angle	α_1'	32.56°
Blade outlet angle	α_2'	-1.52°
Incidence angle	i	-1.56°

Riblet Placement and Sizing.   Three separate

blade configurations were tested: Set #1 had no riblets,

Set #2 had riblets on the suction surface, and Set #3 had

riblets on the pressure surface.   The riblets were applied

to Sets #2 and #3 via 3M Corporation Drag Reduction Film,

also referred to as riblet "tape".   The riblet tape was

applied to the middle three blades of the cascade.   Figure

10 illustrates the riblet placement on the blades.   The

riblets covered the entire surface of the blades of Sets #2

and #3 from the 0.25 chord point to the trailing edge.   The

riblet tape measured 5.5 mils in maximum thickness, and the

V-shaped grooves measured 3 mils in peak-to-valley height

and 3 mils in peak-to-peak distance.   Figure 11 illustrates

the riblet geometry.

20

Analysis using equations (6) and (8) suggests that these riblets were appropriately sized for this application. The results of this analysis are given in Figure 12. The non-dimensional height of the riblets is plotted against blade chord Reynolds number (Re_c) for the leading and trailing edge of the tape as located on blade Sets #2 and #3 (0.25c and 1.00c respectively). The non-dimensional spacing of the riblets (s^+) will be identical due to the symmetry of the riblets. The optimum and extreme h^+ ranges for flat plate viscous drag reduction, identified by Walsh (19), are overlaid on the figure. Although these calculations are only approximate, they indicate that the riblets may have an effect on cascade performance anywhere within $7.0 \cdot 10^4 < Re_c < 4.3 \cdot 10^5$. At a $Re_c \approx 1.5 \cdot 10^5$, the riblets appear to be optimally sized, although the optimum range could vary considerably due to the approximate nature of these calculations.

These calculations were performed using a flat plate approximation, and it is likely that the boundary layer on the suction surface of the blade was somewhat larger than the above boundary layer estimates due to the adverse pressure gradient on that surface. As a result, the estimated riblet h^+ values in Figure 12 are probably somewhat high for blade Set #2. Since the boundary layer thickness on the pressure side of the blade is likely to be somewhat smaller than the flat plate approximation due to the favor-

21.

able pressure gradient on that surface, it is likely that the estimated h^+ values in Figure 12 are somewhat low for blade Set #3. It is also possible that the pressure surface boundary layer on the cascade blades was laminar for a significant fraction of the chord length. If so, the addition of riblets may effect the cascade performance in unexpected ways. The exact expectations regarding the effects of riblets on cascade performance are cited in Chapter V.

Sidewall Boundary Layer Removal. Due to the low aspect ratio of this cascade, sidewall boundary layer control was necessary to inhibit the development of large corner wall vortices over the blades. This control was accomplished through the use of porous sidewalls. The porous region of one sidewall is shown in Figure 6. The material used for these porous sidewalls was 1/16 inch thick, stainless steel, standard sheet stock, produced by Pall Corporation. The suction through the sidewall was performed by a 3.5 horsepower Model 984 Shop Vac industrial duty vacuum.

A set of seven sidewall static pressure taps were drilled into the inlet of the cascade region. The static pressure at each of these taps was monitored in order to detect any static pressure gradients in the flow entering the test section.

Test Section Exit. The exit from the test section was unmodified from previous theses. It extended for over 12

22

inches from the trailing edge of the cascade and utilized
adjustable endwalls for flow balancing. Four pressure taps
were drilled in each of the adjustable endwalls to facili-
tate balancing of the flow through the test section, and
five rows of closely spaced pressure taps lined one side-
wall of the exit at several x locations downstream of the
cascade.

Data Acquisition System

The CTF data acquisition system included the CTF sen-
sors, and all of the devices which manipulated and moni-
tored those sensors. Eighteen pressure transducers, four
thermocouples, an eleven port total pressure rake, and a
1241-10 hot film probe were used. A list of specifications
and serial numbers for the various components is given in
Appendix A.

The data acquisition system consisted of four parts:
the traversing mechanism, the sensors, the sensor electron-
ics, and the central computer. Each of these will be dis-
cussed separately in the following paragraphs.

Traversing Mechanism. The traversing mechanism is
illustrated in Figure 13. The purpose of this mechanism
was to guide the primary data acquisition instrument, be it
a pitot tube, the total pressure rake, or a hot film probe,
to any location in the outlet duct behind the cascade. In
addition, it provided support for four pressure transduc-
ers, including the Scanivalve system.

Movement along the pitch and span axes within the test section was governed by two New England Affiliated Technologies (NEAT) model 310 DC motors, while movement along the axial direction was done by hand. The traverser's position in all three axes was monitored by electronic encoders. These encoders estimated the traverser position, and, hence, the probe position, to within 0.0005 inches in the span and pitch directions and 0.005 inches in the axial direction. The support for the sensor was aerodynamically shaped to minimize buffeting of the probe.

Sensors. The two primary sensors used for this investigation were the total pressure rake, and the two channel hot film anemometer. The pressure rake, designed by Veesart (17), had eleven ports which were each 0.15 inches apart (Figure 13). It was designed to facilitate rapid acquisition of pressure loss data over the central 1.5 inches of the cascade span. A bank of eleven ±0.5 and ±1.0 psi transducers was assembled for use with the rake. These transducers allowed the direct and highly precise measurement of the difference between the CTF stilling tank total pressure and the total pressure registered at each port on the rake.

The hot film probe was a TSI Incorporated 1241-10, "X"-type probe, illustrated in Figure 15. Since an "X"-type probe consists of two separate sensing elements which are approximately normal to each other, it is capable of

24

measuring the flow angle in two dimensions, in addition to its speed and turbulence level. The hot film sensor itself consisted of a fused quartz substrate with a platinum film bonded to the surface. The diameter and length of the sensing element were 0.001 inches and 0.020 inches respectively. The distance between the two elements was 0.05 inches. Details on the calibration and operation of the hot film sensor are given in Appendices C and D respectively.

Sensor Electronics. The hot film probe was connected to a TSI System Intelligent Flow Analyzer (IFA) 100, which was operated in a constant temperature mode. Bridge voltages for the hot film were measured via a twelve bit TSI IFA 200 digital voltmeter with six channel simultaneous sampling capability. The IFA 200 was also occasionally used for thermocouple and pressure transducer measurements when its simultaneous sampling capability was of benefit. However, the majority of pressure measurements were taken via a Hewlet Packard (HP) 3495A Scanner which was connected to a sixteen bit HP 3455A Voltmeter. The greater resolution of the HP voltmeter (16 bit versus 12 bit resolution for the IFA 200) allowed greater precision in the measurement of the voltages from the transducers and thermocouples.

All signals from the sensing elements, with the exception of the four copper constantan thermocouples, were

amplified by Endevco 4423 Signal Conditioners prior to transmission to the TSI or HP volumeters.

Central Computer. A Zenith Z-248 personal computer was used to monitor and control all aspects of instrument calibration and data acquisition. A National Instruments General Purpose Interface Board (GPIB) allowed the computer to interface with the HP scanner and voltmeter. The IFA 200 used Direct Memory Access in order to facilitate rapid data acquisition. The Scanivalve was controlled by the computer via the HP 3495A Scanner.

IV.   Procedure and Assumptions

Procedure

Straight Test Section Work.   Before taking data with
the linear cascade test section in place, baseline perfor-
mance data for the turbulence injector was taken via a
straight-walled test section.   This allowed the direct
measurement of the properties of the test flow immediately
downstream of the turbulence injector.   The magnitude and
distribution of the elevated turbulence levels in the test
flow was analyzed.   In addition, pressure loss and velocity
profiles at several stations downstream of the turbulence
injector were constructed.

Blade Selection.   The molded epoxy blades that were
available for this investigation were not completely uni-
form in surface roughness and shape.   This is attributable
to imperfections in the molding process.   As a result, a
large number of blades were visually screened, and only
blades with similarly smooth surfaces and identical shapes
were used as test specimens.

Finally, in order to remove any possible effects of
blade-to-blade differences between the test specimens, the
same blades were used for both the Set #1 and Set #2 tests.
Since it was impractical to attempt to remove the riblet
tape from the suction surfaces of Set #2 once it had been
applied, it was necessary to use a different set of blades

for Set #3. However, before applying riblet tape to the pressure surfaces of Set #3, their cascade performance was first examined with no riblets in order to verify similarity with Set #1.

Data Acquisition. The general philosophy for data acquisition for this investigation can be summarized as follows. First, all pressure transducer signals were checked for drift and then corrected prior to every data run. Second, the test section was re-balanced for every change in test section Reynolds number and for every new blade configuration. Third, the hot film anemometer frequency response and operating temperature were adjusted prior to every hot film run. The frequency adjustment was performed by using an oscilloscope to monitor the anemometer voltage response to a square wave test signal. Adjustments were made to the anemometer cable and bridge compensations in order to minimize the signal response time. Fourth, ambient temperature and barometric pressure were checked and corrected approximately every two hours, unless a significant change in laboratory room temperature warranted an immediate update.

In regards to test section "balancing", a well balanced test section is one in which the test flow is turned only by the aerodynamic action of the cascade and not by the test section endwalls. An out-of-balance test section will force the test flow in some direction other than that

which would be determined by the cascade alone. Therefore, the endwalls of an unbalanced test section will impose a pitchwise static pressure gradient in the test flow within the cascade.

For this investigation, the test section was balanced by raising and/or lowering the movable endwalls which were part of the test section exit. Three separate criteria were used to determine if the section was balanced. First, the seven static pressure ports which cross the inlet to the cascade were checked for a pressure gradient in that region. Second, the 19 static pressure ports immediately downstream of the center three blades of the cascade were checked for "periodicity." Periodicity refers to the regular and repeating variation in flow properties from one cascade channel to another. Finally, although not strictly a balancing requirement, the four static pressure ports in each of the movable endwalls were checked to assure that the exit static pressure from the cascade was uniform in the axial direction and approximately equal to the ambient pressure in the laboratory. A large pressure difference between two opposite ports in the endwalls would indicate a static pressure gradient downstream of the cascade. Any such significant pressure gradients were eliminated prior to data acquisition.

In order to assure the repeatability of the data in this thesis, every reported data point was re-checked with

29

a separate data acquisition run. Since these reruns were only intended to be checks of the primary data, test section balance was not refined, and the pressure transducers were not corrected for drift prior to data acquisition. However, since the measured cascade performance was relatively insensitive to these parameters, all of the trends noted in Chapter V, Discussion of Results, were consistently repeatable using this technique.

Test Grid. Data was taken at one chord length downstream of the cascade ($x = 1.0c$). Pressure rake data was taken at eleven equally space spanwise locations across the middle 1.5 inches of the blade as illustrated in Figure 16. Figure 16 was modified from Veesart (17: 4-8). Hot film data was taken at $z = -0.3$, 0, and 0.3 inches. Finally, all data, both pressure rake and hot film, was taken at 0.01 inch pitch intervals across the entire center blade spacing ($-0.66 < y < 0.66$ inches), yielding a total of 134 pitchwise data points.

Assumptions. The test flow along the centerline of the cascade is assumed to be two dimensional. Since the measured AVDR values for all test conditions ranged from 0.94 to 1.04, this appears to be a reasonable assumption. Also, since the balance of the test section was constantly monitored and adjusted for each change in test conditions, the test section is assumed to be balanced for all of the data presented herein.

V.   Discussion of Results

Approach

A preliminary examination of the two-dimensionality of the flow through the cascade will establish the set of assumptions to be applied to the rest of the results in this chapter. Next will come the formal analysis of experimental results. Prior to each section of the results discussion, the expectations regarding the effects of riblets on the cascade performance will be presented. The remainder of the discussion will then be couched in terms of those expectations. The performance of the cascade will first be quantified in terms of gross parameters, including total pressure loss coefficient, turning angle, and static pressure rise. The discussion will then become primarily qualitative in nature, with an analysis of the most interesting wake velocity profiles. The specific cases to be so addressed will be identified from the quantitative discussion.

Cascade Two-Dimensionality

Before any comparisons can be made between two sets of data, the state of the flow through the cascade must be well established for both cases. Of specific concern in this analysis is the magnitude of the influence of the corner wall vortices on the flow through the cascade. As mentioned in Chapter III, these vortices have been shown to

draw air from the cascade sidewalls onto the suction sur-
face of the blades. This forces the air that was already
on the blade towards the centerline (5:54-56). If the
corner wall vortices are small with respect to the overall
span of the blades, this effect will be negligible and the
AVDR through the cascade will approach unity. However, if
they are large, the mass flow near the blade's centerline
will increase significantly and the AVDR will exceed unity.

The value of AVDR was measured for every test case.
These values are plotted in Figures 17 and 18 for the low
and high turbulence level test cases respectively. An
attempt was made during data acquisition to maintain the
AVDR at a relatively constant level from one test to anoth-
er. This was achieved by varying the amount of vacuum
applied to the porous sidewalls. Although Figures 17 and
18 indicate some measure of success in that effort, the
AVDR still varied from as low as 0.94 at the lowest Rey-
nolds numbers to 1.04 at the highest Reynolds numbers.
This indicates that the influence of corner wall vortices
varied for test conditions of differing blade chord Rey-
nolds numbers. This limits the type of comparisons that
can be made in the data for this thesis. Specifically,
while it is possible to directly compare test results from
different blade sets which were taken at the same Reynolds
number, it is not appropriate to make direct comparisons of
test data taken at widely differing Reynolds numbers. It

is still possible to make conclusions regarding the effects of riblets on cascade performance at each of the specific Reynolds number conditions tested. In addition, Scholz stipulated that an AVDR between 0.8 and 1.2 was acceptable for the assumption of quasi-two-dimensional flow at the cascade centerline (18:489). Since the AVDR values given in Figures 17 and 18 lie well within this range, the observed effects of the riblets in the following data should reflect two-dimensional behavior.

One method of determining the extent of the region of the corner vortex influence is to examine the shape of the wake coming off the trailing edge of the blade. In particular, a contour plot of the loss in total pressure in the y $- z$ plane downstream of the blade revealed the presence of the corner vortices quite clearly. Figure 19 contains two such plots, which were compiled from data taken at the $x =$ $1c$ plane. This data was for the center blade of Set #1 and represents local values of the total pressure loss coefficient. In both plots, the blade wake is indicated by increased values of the pressure loss. Figure 19a illustrates the wake at a blade chord Reynolds number of approximately 70,000, and shows very little variation in shape or depth in the z direction. However, for the same configuration at $Re_c \approx 430,000$ (Figure 19b), large vortices dominated the lower half of the wake for nearly the entire span of the blade. Only the region at the very center span of the

wake ($z = 0$) was free from the vortices' immediate influence.

Figure 19 illustrates the two extremes in the capability of the available sidewall suction to inhibit the growth of three-dimensional influences through the cascade. For the low Reynolds number cases, the porous sidewalls were able to remove enough of the boundary layer to nearly eliminate vortex growth. In fact, the AVDR values of approximately 0.95 for those test cases indicate that more suction was applied than was necessary to maintain the AVDR near one. However, for the highest Reynolds number cases, the porous sidewalls were practically ineffective at inhibiting vortex growth. Therefore, in order to minimize the influence of the corner wall vortices on the test data, the spanwise sampling region for data reduction was restricted to the centerline ($z = 0$) of the cascade.

Total Pressure Loss Coefficient

Each blade set was tested over a Re_c range of approximately 70,000 to 430,000. In addition, cascade performance was evaluated for flows with both low and high turbulence levels. The elevated turbulence levels were approximately three percent, while the low turbulence levels were approximately 0.1 to 0.2 percent. All data for the remainder of this discussion will be separated between the low and high turbulence cases.

The application of riblets to either surface of the

34

cascade blades was expected to decrease the cascade total
pressure loss coefficient. Based on the riblet sizing
discussion of Chapter III, this reduction in ω was expected
to take place anywhere within the tested blade chord Rey-
nolds number regime.

Regarding Reynolds number effects, Gostelow (7) and
Roudebush (14) observed that two-dimensional cascade per-
formance generally degrades with decreasing blade chord
Reynolds number. This degradation is normally very slight
until the Reynolds number drops below some distinct value.
Below this value, cascade losses increase markedly for
moderate to highly loaded cascades, due to laminar separa-
tion on the blades. Roudebush reported that for a cascade
similar to the one used in this investigation, this separa-
tion Reynolds number was approximately $2.0 \cdot 10^5$ (14:164-
167). Therefore, for the data of this investigation, one
would expect to see relatively constant total pressure loss
performance with Reynolds number down to $Re_c \approx 2.0 \cdot 10^5$.
Below this Re_c value, an increase in ω was expected.

Figures 20 and 21 summarize the mass averaged total
pressure loss coefficient data for all test conditions.
The total pressure losses generally increase slightly with
Reynolds number for the low turbulence level data of Figure
20. This increase is more significant in the high turbu-
lence level data of Figure 21. In both cases, this in-
crease in ω is attributable to effects of corner wall

35

vortex development at higher Reynolds numbers, due to inadequate boundary layer removal. Non-ideal Reynolds number dependant trends such as this indicate that the absolute magnitude of the experimental results reported in this thesis are not ideally two-dimensional. However, since the AVDR of all the data is approximately close to one, the *trends* in the data from one blade set to another and at any given Reynolds number are valid.

The data of Figure 20 behaved as expected with two exceptions. First, at high Reynolds numbers, the suction surface riblets failed to reduce total pressure losses through the cascade as did the pressure surface riblets. The reason for this is uncertain; however, it may be at-tributable to the interaction of the suction surface rib-lets with the developing corner wall vortices. In fact, the suction surface riblets offered no discernable reduc-tion in ϖ at any Re_c. On the other hand, the pressure surface riblets reduced ϖ by approximately 10 percent for $Re_c \geq 3.0 \cdot 10^5$. This may indicate that these riblets re-duced the skin friction drag on that surface. The other unexpected result in Figure 20 was that the pressure sur-face riblets significantly increased total pressure losses at the lowest Re_c while the other two blade sets continued to experience a decrease in ϖ all the way down to $Re_c \approx 7.0 \cdot 10^4$. At these low Reynolds numbers, it is likely that a laminar boundary layer was present on the majority of the

pressure surface of the blade. It is therefore possible that the riblets were interfering with this boundary layer in such a way as to increase ω. Blade Sets #1 and #2 did not experience a similar increase in ω.

At high Reynolds numbers, the elevated turbulence level data of Figure 21 demonstrates the same behavior as the low turbulence level data. At high Re_c, the pressure surface riblets reduced ω by nearly 15 percent, whereas the suction surface riblets were largely ineffective. However, in contrast to the data in Figure 20, all three blade sets experienced the increase in ω that is characteristic of low blade chord Reynolds numbers such as suggested by Gostelow (7) and Roudebush (14).

In theory, high freestream turbulence levels should make a cascade less susceptible to laminar separation effects. The fact that this low Re_c data suggests otherwise supports the conclusion that some other mechanism is responsible for the increase in ω in Figure 21 at $Re_c \approx 7.0 \cdot 10^4$. This mechanism may involve a change in the effective skin friction coefficient of the cascade blades at high turbulence levels, or it may involve irregularities introduced into the flow by the turbulence injector. Whatever the mechanism, the clear trend is that, at low turbulence levels and low Reynolds numbers, pressure surface riblets significantly increase the cascade total

37

pressure losses. This increase is on the order of 30 percent. Regarding the data at intermediate Reynolds numbers in Figures 20 and 21, no consistent trends were discernable.

The magnitude of ω at $Re_c \approx 4.3 \cdot 10^5$, given in Figures 20 and 21, corresponds closely with the values reported by DeCook (5) for the same cascade. DeCook's total pressure loss coefficient data is on the order of 0.35 to 0.4 at the $x = 1.0c$ location (5:68). The corresponding values given in Figures 20 and 21 range from 0.35 to 0.56. The differences between DeCook's data and the data presented in this thesis are due primarily to the fact that the sidewall boundary layer control used for this investigation was less effective at high Reynolds numbers. DeCook used upstream sidewall slots instead of porous sidewalls (5). Since DeCook's boundary layer control was more effective, his data did not reflect the cumulative increase in ω with Reynolds number that was present in this study. Therefore, his ω values are slightly lower.

Turning Angle

Assuming uniform two-dimensionality for all test cases, the turning angle performance of the cascade was expected to remain relatively constant for the intermediate to high blade chord Reynolds numbers. At the lowest Reynolds numbers, the turning angle was expected to decrease as a result of the laminar boundary layer separation phe-

38

nomenon reported by Roudebush (14). Further, this decrease in turning angle should coincide with the increase in $\bar{\omega}$ reported in the previous section.

Regarding the effects of riblets, it was expected that the suction surface riblets would have a small but positive effect on turning angle at higher Reynolds numbers. Since riblets have been shown to delay separation in diffusers (12), the suction surface riblets were projected to decrease the extent of the separated region near the trailing edge of the suction surface of the blade. This would tend to increase the net turning angle through the cascade.

Pressure surface riblets were expected to have a smaller effect on turning angle than the suction surface riblets. Since pressure surface boundary layers are not prone to separation, the primary effect of pressure surface riblets would be limited to the reduction of viscous drag. Although this would tend to increase the turning angle, the magnitude of this increase would be relatively small.

Figures 22 and 23 depict the mass averaged turning angle that was measured at each test condition. These figures indicate, once again, that uniform two-dimensionality was not achieved over the span of Reynolds numbers tested. The turning angle generally decreased with increasing Reynolds number for $Re_c \geq 2.0 \cdot 10^5$. This is attributable to the increasing influence of corner wall vortices at high Re_c. The two counterrotating vortices

that propagate downstream from each blade in the cascade
rotate in a direction that tends to depress the turning
angle at the test section centerline. As these vortices
become stronger at higher Reynolds numbers, the measured
turning angle at the centerline of the cascade progressive-
ly decreases. It is also possible that this decrease in
turning angle is related to the increase in total pressure
losses noted in Figures 20 and 21.

At the lowest Reynolds numbers, the turning angle
tended to decrease as expected. This decrease was much
more pronounced for the high turbulence level data of
Figure 23 than for the low turbulence level data of Figure
22. This corroborates the trend noted in the ω data that
elevated freestream turbulence degraded cascade performance
at low Re_c. Since the low turbulence level data generally
does not exhibit such a significant degradation in perfor-
mance, the evidence suggests that the turbulence injector
modified the flowfield within the cascade in an unexpected
manner. If the degradation in cascade performance at very
low Re_c is due to boundary layer separation over the suc-
tion surface of the blades, as suggested by Roudebush (14),
then the turbulence injector may have increased the flow
incidence angle at the leading edge of the test blade.
This would encourage premature separation from the suction
surface of the blade; and, therefore, increase the total
pressure deficit in the blade wake. The turning angle

would tend to decrease in such a scenario as well, as was observed. However, this is not the only possible explanation. It is possible that the change in freestream turbulence level increased the size of the boundary layer on the pressure surface of the blade, therefore degrading cascade performance. It is also possible that the physical scale of the turbulence introduced by the turbulence injector interacted with the dimensions of the CTF test section in such a manner as to influence the performance of the cascade at very low blade chord Reynolds numbers. Finally, it may be that some combination of the above effects is taking place.

As a general rule, the difference in turning angle between the three blade sets at any given Reynolds number was very small. Normally this difference was no larger than ± 0.2 to 0.3 degrees. During data acquisition, the observed repeatability of each of the turning angle data points was approximately ±0.15 degrees. Therefore, the majority of the points on Figures 22 and 23 lie within or near this interval.

However, three consistent trends in the turning angle data were apparent. First, the suction surface riblets increased turning angle at very high Reynolds numbers as expected, particularly at low freestream turbulence levels. This increase was on the order of 1 to 2 percent. Second, both the pressure and suction surface riblets increased

turning angle for the $2.0 \cdot 10^5 \leq Re_c \leq 3.0 \cdot 10^5$ range in Figure 23. Again, the magnitude of this increase was approximately 1 to 2 percent. This same trend is noted in the low freestream turbulence data of Figure 22, except to a lesser degree. Third, pressure surface riblets *decreased* turning angles at low Reynolds number and high turbulence level conditions. This was unexpected, and is a continuation of the anomalous behavior of the cascade at very low Re_c. An explanation for this behavior remains elusive. Nevertheless, the consistent repeatability of these low Re_c results warrants continued attention.

Pressure Rise Coefficient

The static pressure ahead of and behind the cascade was monitored by two ±2.0 psi Statham transducers. The upstream measuring point was three inches ahead of the cascade, and the downstream measuring point was approximately two inches behind it. These pressures were differenced to arrive at the static pressure rise through the cascade. The non-dimensional static pressure rise coefficient, C_p, is determined by dividing this pressure rise by the incoming dynamic pressure, q_1. The more efficient a given cascade becomes, the higher its C_p value will be. The measured values for C_p are plotted in Figures 24 and 25.

The C_p performance of an ideal two-dimensional cascade will remain approximately constant with respect to Reynolds

42

number. As was the case with ⍺ and turning angle, only at very low Re_c would one expect the static pressure rise coefficient performance of the cascade to degrade.

Riblets were expected to increase the C_p performance of this cascade because of the predicted ability of riblets to increase turning angle and decrease pressure losses. The following equation illustrates the functional relationship that governs this rise in C_p for a two-dimensional cascade:

$$C_p = 1 - cos^2\alpha_1 - \bar{\omega}$$ (9)

In order to arrive at this equation, equation (2) was first corrected for the total pressure losses through the cascade by subtracting the loss in total pressure from the right-hand-side. Then, α_2 was set to zero, thus making α_1 the air turning angle. Finally, both sides of the equation were divided by the upstream dynamic pressure.

Unfortunately, equation (9) applies only to the C_p value that would be measured behind a two dimensional cascade. The C_p measuring stations for this investigation were located on the cascade sidewalls, three inches upstream and two inches downstream of the cascade. As demon-strated repeatedly, the flow across the span of this cascade was often strongly three-dimensional. According to Erwin and Emory (6) the measured C_p values for such a cascade will often bear little resemblance to those pre-

43

dicted by equation (9), particularly if one were to use the measured two-dimensional turning angle and total pressure loss coefficient at the cascade centerline for the calculation.

The measured C_p values from Figures 24 and 25 decrease continuously with increasing Re_c. There were two primary reasons for this trend. First was the increase in total pressure losses through the cascade with Reynolds number. Second was the decrease in flow turning angle.

In regards to the total pressure losses, the ω values presented in Figures 20 and 21 represent the total pressure losses measured at the centerline of the cascade. This choice of the spanwise sampling region removed the direct influence of the large pressure loss regions associated with the corner wall vortices which are illustrated in Figure 19. If the spanwise sampling region for ω is increased to include the full range of the total pressure rake (± 0.75 inches), ω increases to approximately 0.08 at the highest Reynolds numbers. This is a dramatic increase from the values reported in Figures 20 and 21, and is very close to the ω values reported in DeCook (5) for his suction off, baseline blade configuration. If the spanwise sampling region were increased to include the entire span of the test section (± 1.0 inches), the value for ω would likely increase considerably. Therefore, the total pressure loss coefficient for the full span of the test section

increased approximately a full tenth of a point from the lowest Re_c test cases to the largest Re_c cases. According to equation (9), this would account for a decrease in C_p of roughly the same amount ($\Delta C_p \approx -0.1$).

The second contributor to the decrease in C_p with Reynolds number was the decrease in turning angle through the cascade. The changes in turning angle noted in Figures 22 and 23 were measured at the centerline of the cascade. Although these values likely represent the approximate turning angles of a two dimensional cascade, they do not represent the spanwise average of the turning angle through this test section. Although this spanwise average was never measured directly, it can be inferred from the placement of the movable endwalls in the test section exit. As noted in Chapter III, these endwalls were positioned so as not to force the flow exiting the cascade in a direction other than that which would have been determined by the cascade alone. Therefore, these endwalls should have been approximately parallel to the exiting airflow. Assuming a well balanced test section, the relative positions of the endwalls for two different test cases can then be used to obtain a rough estimate the difference in the span averaged turning angle between those cases. By measuring the location of the endwalls with respect to the cascade, the estimated span averaged turning angles for the $Re_c \approx 7.0 \cdot 10^4$ test cases were approximately 30°. For the $Re_c \approx$

$4.3 \cdot 10^5$ cases, this angle decreased to approximately 27°.
In order to estimate this effect on equation (9), $\cos^2(27^\circ)$
can be subtracted from $\cos^2(30^\circ)$. This yields a ΔC_p due to
the change in turning angle of approximately -0.04.

Combining the influences of σ ($\Delta C_p \approx -0.1$) and test
section turning angle ($\Delta C_p \approx -0.04$), the total change in C_p
from $Re_c \approx 7.0 \cdot 10^4$ to $Re_c \approx 4.3 \cdot 10^5$ is estimated to be
approximately -0.14. This corresponds quite closely to the
measured difference in the C_p data presented in Figures 24
and 25 from $Re_c \approx 7.0 \cdot 10^4$ to $Re_c \approx 4.3 \cdot 10^5$.

The effects of riblets on the measured C_p did not
follow the two-dimensional cascade expectations. This was
not a surprise, particularly in light of the preceding
discussion on the large three-dimensional effects on the
measured C_p performance of the cascade. At high Reynolds
numbers where the riblets demonstrated two-dimensional
effectiveness, these three dimensional effects (i.e., the
corner wall vortices) were predominant. In both Figures 24
and 25, the data at low Reynolds numbers exhibited consid-
erable scatter, and no conclusions can be drawn from it.
The only recognizable trend in these figures is the consis-
tent decrease in C_p at high Reynolds numbers due to the
presence of suction surface riblets. There are no indica-
tions in the two-dimensional σ or turning angle data that
this blade set should decrease C_p in such a manner. This
indicates that the suction surface riblets may have

interacted with the developing corner wall vortices in such a way as to increase the vortices influence on the static pressure rise through the test section. Although consistent, this change in C_p is relatively small. The decrease in C_p never exceeds 0.01.

Wake Velocity Profiles

The only expectation regarding the influence of riblets on the wake velocity profiles involved the relative sizes of the suction and pressure surface boundary layers at the trailing edge of the blade. If the riblets decreased the size of the boundary layer on either surface, this should be identifiable by a shift in the wake velocity profile. This is a result of the smaller relative size of that portion of the wake with respect to the portion of the wake emanating from the other surface of the blade. This would cause a net decrease in the size of the entire wake, and, therefore, a decrease in the total pressure loss coefficient. With this in mind, careful attention will be paid to the high Reynolds number, pressure surface riblet data. Since the ω data for that case showed a significant decrease (note Figure 20), this is a likely candidate for a change in the wake velocity profile.

The wake velocity profiles were very similar for the majority of test cases. The non-dimensional velocity profiles of the centerline wakes for several test cases are given in Figures 26 - 31. The velocities were non-dimen-

sionalized by dividing them by the corresponding inlet velocity to the cascade, and each plot contains simultaneously plotted data for all three blade sets. Figures 26 - 28 are low turbulence cases while Figures 29 - 31 are high turbulence cases. The data in Figures 26 and 29 was taken at blade chord Reynolds numbers of approximately 70,000. The data in Figures 27 and 30 was taken at $Re_c \approx$ 250,000. Finally, the data in Figures 28 and 31 was taken at $Re_c \approx$ 430,000. On all of the profiles, the left half of the curve (negative pitch) is for that portion of the wake and passage flow adjacent to the suction surface of the blade, while the right half (positive pitch) is for that adjacent to the pressure surface.

Several general trends in the data are evident. First, the scatter of the data is reduced as Reynolds number increases because of the limitations of instrument sensitivity at very low velocities (note Figures 26-28). The primary difference between the low and high turbulence level plots is in the pitchwise thickness of the wakes. In general, the wakes were thickened by the elevation in free stream turbulence. This was expected since elevated free-stream turbulence will increase the efficiency of the momentum transport between the low speed air in the wake and the higher speed external air. In addition to becoming thicker, the velocity deficit of the wake decreased. The velocity deficit is defined as the maximum difference

between the velocity at any point in the wake and the freestream velocity.

In some cases, riblets had a marked effect on the shape and placement of the wake. In Figure 27, a small shift in the negative pitchwise direction, or to the left of the plot, is noted for the pressure side riblets. This shift was even more pronounced for the highest Reynolds number data in Figure 28. In both cases, the shift was greater on the right half, or pressure side, of the wake. It appears that, as expected, the pressure side riblets reduced the thickness of the wake emanating from the pressure side of the blade. This resulted in a reduction in the size of that half of the wake, and, therefore, a net shift towards the suction side of approximately 0.05 inches. Consequently, the thickness of the wake was less than that for blade sets #1 and #2, becoming progressively more so as Re_c increased. As suggested above, it appears that this was responsible for the decreased total pressure losses noted for the highest Reynolds number tests of Set #3 (Figure 19). Although this blade set reduced ω at high Reynolds numbers, it did not increase flow the turning angle. It may be that the net shift in the wake's placement in the negative pitchwise direction eliminated any potential increase in turning angle that may have resulted from the increased efficiency. This same scenario is repeated for the turbulent flow data of Figures 29 - 31.

Summary

In general, riblets were expected to decrease ω, increase turning angle, and increase C_p. Due to the relative size of the riblets with respect to the estimated size of the boundary layers on the blades, the riblets were expected to be effective anywhere within the tested Reynolds number regime. Since the boundary layer is normally thicker on the suction surface of a blade than on the pressure surface, the influence of the pressure surface riblets was expected to become evident at lower Re_c than the suction surface riblets.

The primary trend that was noted in the data was that pressure surface riblets were most effective at decreasing pressure losses through the cascade, whereas suction surface riblets tended to improve turning angle. As noted in the wake velocity profile data, the ω reducing effects of the pressure surface riblets were apparently due to a decrease in the size of the boundary layer on the pressure surface of the blades. Few conclusions can be drawn from the C_p data. The influence of secondary flows in the test section dominated the C_p performance of the cascade as measured from the test section sidewalls.

In general, riblets appear to offer the potential to enhance axial compressor performance if properly sized to interact favorably with the blade boundary layers. The flat plate approximation of laminar sublayer thickness

proved effective at estimating the approximate Reynolds
number regime in which the riblets should be beneficial to
cascade performance.

VI.   Conclusions and Recommendations

Conclusions

All three goals of this thesis, as cited in Chapter I, were achieved. First, it was determined that the effects of riblets on cascade performance were measurable. Second, the specific test conditions under which the riblets altered the performance of the cascade were established. Third, the magnitude of these effects were quantified, and the qualitative impact on cascade performance was resolved.

The pressure surface riblets decreased ϖ by approximately 10 percent for $Re_c \geq 3.0 \cdot 10^5$ and at low freestream turbulence levels. This decrease was approximately 15 percent for $Re_c \approx 4.3 \cdot 10^5$ at high turbulence levels. However, these riblets *increased* ϖ by approximately 30 percent at $Re_c \approx 7.0 \cdot 10^4$ at low turbulence levels. Suction surface riblets, although ineffective at decreasing ϖ, increased flow turning angle by approximately 1 percent at $Re_c \approx 4.3 \cdot 10^5$ for both turbulence level conditions. The only identifiable trend in the C_p data was that suction surface riblets decreased C_p for $Re_c \geq 2.0 \cdot 10^5$. The ϖ and turning angle data taken at the centerline of the cascade suggest that this degradation in static pressure rise is due to the interaction of the suction surface riblets with the developing corner wall vortices. Therefore, large secondary flows in the cascade appear to eliminate the potential effective-

ness of riblets to enhance the static pressure rise.

Recommendations

As is typical with a thesis of this nature, more questions were asked than were answered during the course of this investigation. This thesis covered a very broad topic which is open to a considerable number of more specific investigations. Several of these detailed efforts are described below.

Combined Pressure and Suction Surface Riblets. Some of the data acquired during the course of this investigation suggests that further improvements could be achieved in cascade performance through the simultaneous application of riblets to both sides of the cascade blades. The dimensions of these riblets would likely have to differ in order to accommodate the different size boundary layers on the pressure and suction sides of the blade.

Riblets at Various Incidence Angles. One of the greatest potential benefits that riblets may offer to cascade performance was not investigated in this thesis. Riblets have been shown to significantly delay separation in a diffuser. It is reasonable to assume that riblets may delay separation in a highly loaded cascade at high incidence angles as well. If this is true, riblets may be a potent mechanism for preventing compressor stall at off-design conditions. A variable incidence study would address this issue.

53

<u>Parametric Investigation of Various Riblet Geometries</u>.
This study analyzed the effects of only a single type of
riblet. It is possible that riblets of different shapes and
sizes may provide more robust capabilities to improve cas-
cade performance. Such an investigation would likely have
to limit itself to only one or two specific Reynolds number
conditions in order to limit the magnitude of the required
data acquisition and reduction.

<u>Combined Effects of Riblets and Trailing Edge Crenela-
tions</u>. It has been demonstrated that trailing edge crenela-
tions can decrease the losses and increase the turning angle
through a linear cascade. This study demonstrated that
riblets have the same effect under certain conditions. The
combined effects of riblets and crenelations may be cumula-
tive.

<u>Blade Surface Boundary Layer and Static Pressure Inves-
tigation</u>. Considerable insight into the mechanisms behind
many of the riblet effects noted during this investigation
could be gained through measurement of the blade surface
boundary layer thicknesses and static pressure distribu-
tions. In particular, such an investigation would reveal
the presence of laminar boundary layer separation and would
evaluate the effects of riblets on blade boundary layer
thickness.

References

1. Abbot, Ira H., and Albert E. von Doenhoff. _Theory of Wing Sections_. New York: Dover Publications, Inc., 1959.

2. Allison, Dennis M. _Design and Evaluation of a Cascade Test Facility_. MS Thesis GAE/AA/81D-2. School of Engineering, Air Force Institute of Technology (AU), Wright-Patterson AFB OH, June, 1982.

3. Bacher, E. V., and C. R. Smith. "Turbulent Boundary-Layer Modification by Surface Riblets," _AIAA Journal, 24-8_: 1382-1384 (August 1986).

4. Bradshaw, P. _An Introduction to Turbulence and its Measurement_. New York: Pergamon Press, 1971

5. Decook, Steven J. _Experimental Investigation of Trailing Edge Crenelation Effects on Losses in a Compressor Cascade_. Unpublished thesis. School of Engineering, Air Force Institute of Technology (AU), Wright-Patterson AFB OH, December, 1991.

6. Erwin, John R., and James C. Emery. _Effect of Tunnel Configuration and Testing Technoque on Cascade Performance_. NACA TN-2028. Washington: National Advisory Committee for Astronautics, 1950.

7. Gostelow, J. P. _Cascade Aerodynamics_. New York: Pergamon Press, 1984.

8. Kays, William Morrow and Michael E. Crawford. _Convective Heat and Mass Transfer_. New York: McGraw Hill, 1980.

9. Kuethe, Arnold M., and Chuen-Yen Chow. _Foundations of Aerodynamics: Bases of Aerodynamic Design_ (Third Edition). New York: John Wiley and Sons, 1976.

10. Lieblein, Seymor. "Experimental Flow in Two-dimensional Cascades," _Aerodynamic Design of Axial Flow Compressors (Revised)_, edited by Irving A. Johnson and Robert O. Bullock. NASA SP-36. Washington: National Aeronautics and Space Administration, 1965,

11. Lieblein, Seymor, and William H. Roudebush. _Low Speed Wake Characteristics of Two-Dimensional Cascade and Isolated Airfoil Sections_. NACA TN-3771. Washington: National Advisory Committee for Aeronautics, 1956.

12. Martens, Mathan W. _Effect of Riblets Upon Flow Separation In a Subsonic Diffuser_. MS Thesis GAE/AA/88D-23, School of Engineering, Air Force Institute of Technology (AU), Wright-Patterson AFB OH, December, 1988.

13. Reagan, Michael K. _Effect of Riblets on Pressure Recovery in a Straight-Walled Diffuser_. MS Thesis GAE/ENY/90D-21. School of Engineering, Air Force Institute of Technology (AU), Wright-Patterson AFB OH, December, 1990.

14. Roudebush, William H., and Seymour Lieblein. "Viscous Flow in Two-dimensional Cascades," _Aerodynamic Design of Axial Flow Compressors_ (Revised), edited by Irving A. Johnson and Robert O. Bullock. NASA SP-36. Washington: National Aeronautics and Space Administration, 1965.

15. Schlicting, H. _Boundary Layer Theory_ (Seventh Edition). New York: McGraw Hill, 1979.

16. Scholz, Norbert. _Aerodynamics of Cascades_, AGARD-AG-220. Neuilly sur Seine: Advisory Group for Aerospace Research and Development, 1977.

17. Veesart, J. L. _Wake Dissipation and Total Pressure Loss in a Two-Dimensional Compressor Cascade with Crenelated Trailing Edges_. MS Thesis GAE/AA/89J-3. School of Engineering. Air Force Institute of Technology (AU), Wright-Patterson AFB OH, June 1989.

18. Walsh, Micheal J. "Riblets as a Viscous Drag Reduction Technique," _AIAA Journal, 21-4_: 485-486 (April 1983).

19. Walsh, M. J., and A. M. Lindeman "Optimization and Application of Riblets for Turbulent Drag Reduction," _Proceedings of the AIAA 22nd Aerospace Sciences Meeting_. Paper No. 84-0347. New York: American Institute of Aeronautics and Astronautics, 1984.

20. Wieck, Timothy D. _Effect of Riblets on Flow Separation From a Cylinder and an Airtoil in Subsonic Flow_. MS Thesis GAE/ENY/89D-40. School of Engineering, Air Force Institute of Technology (AU), Wright-Patterson AFB OH, December, 1989.
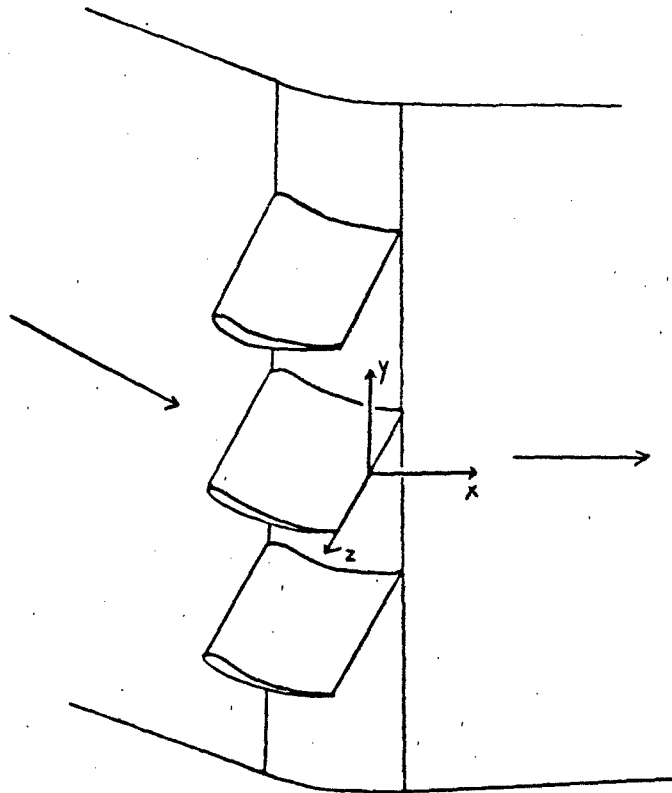
Figure 1. Cascade Coordinate System
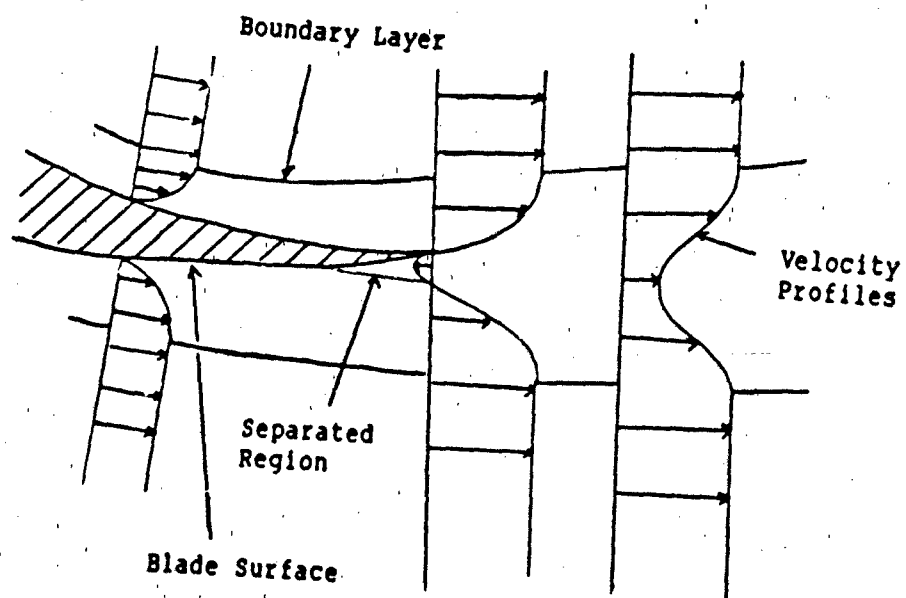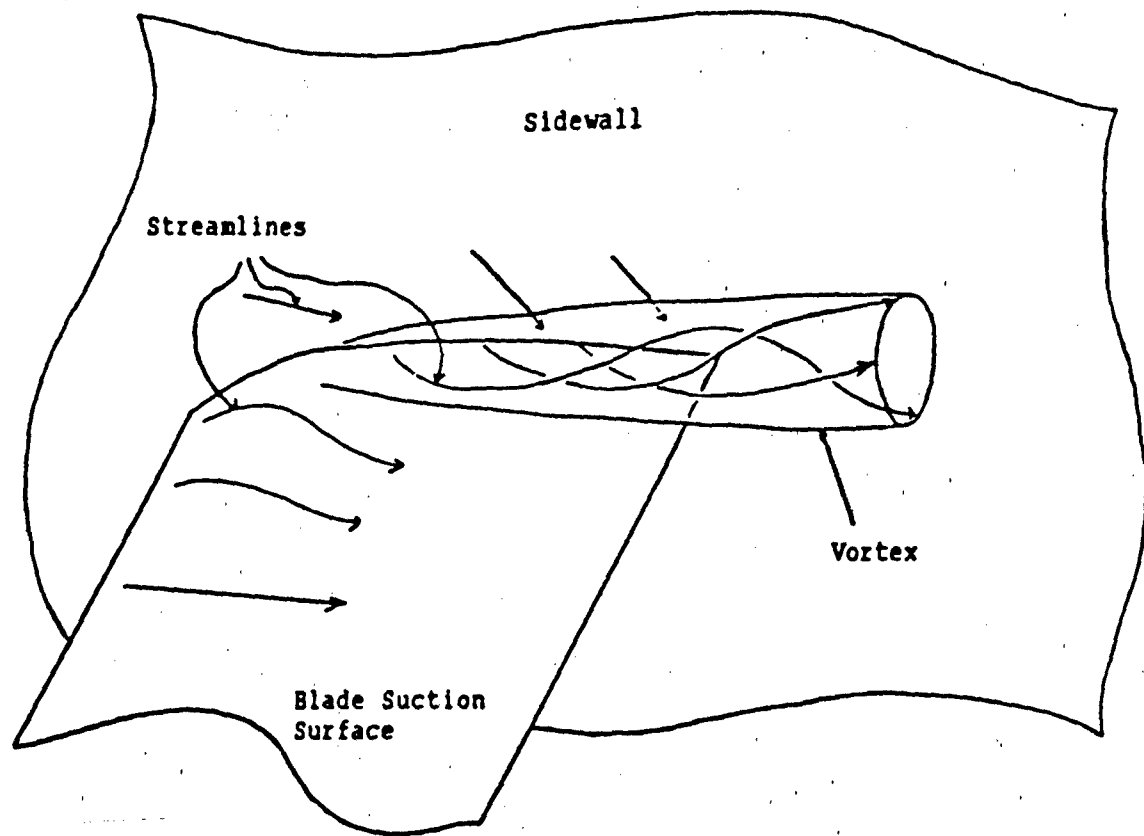

Figure 2. Formation of Blade Wake
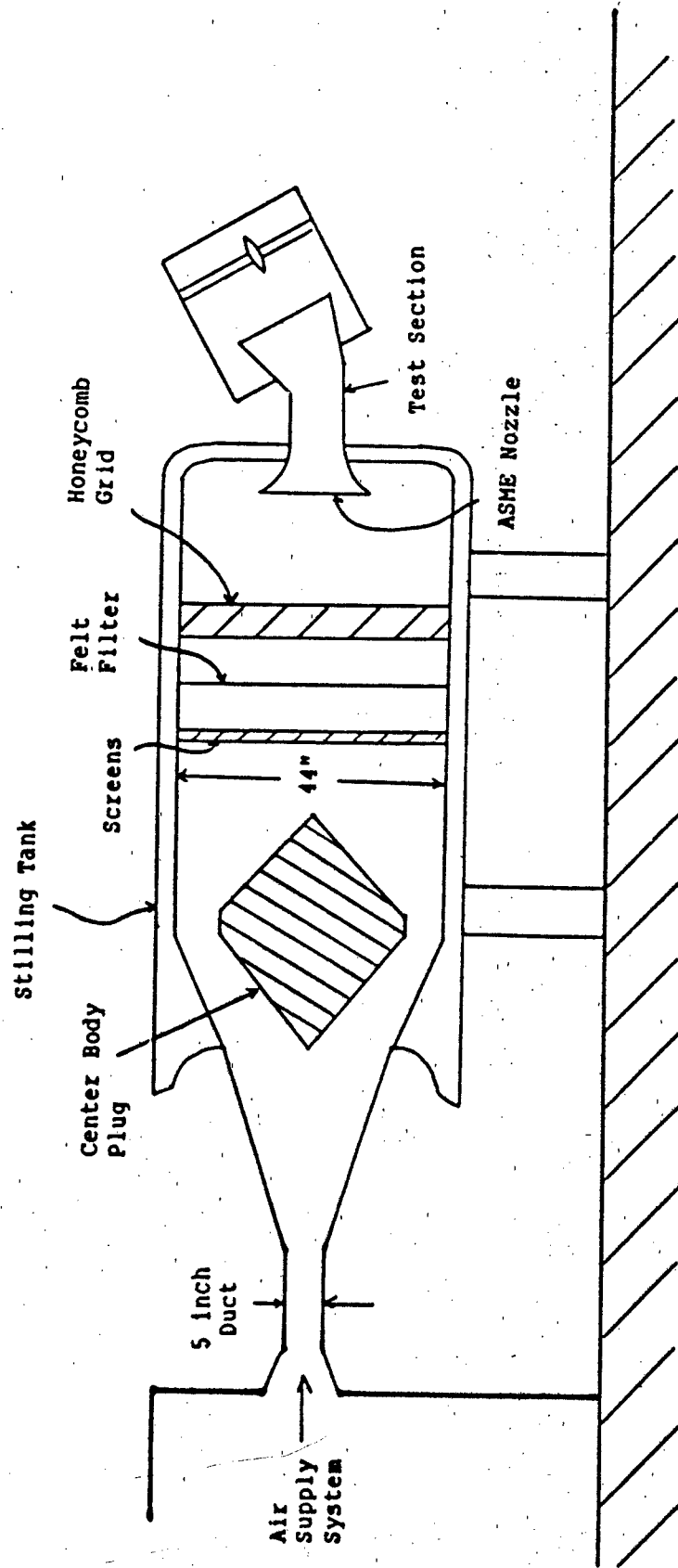
Figure 3. Corner Wall Vortex Development
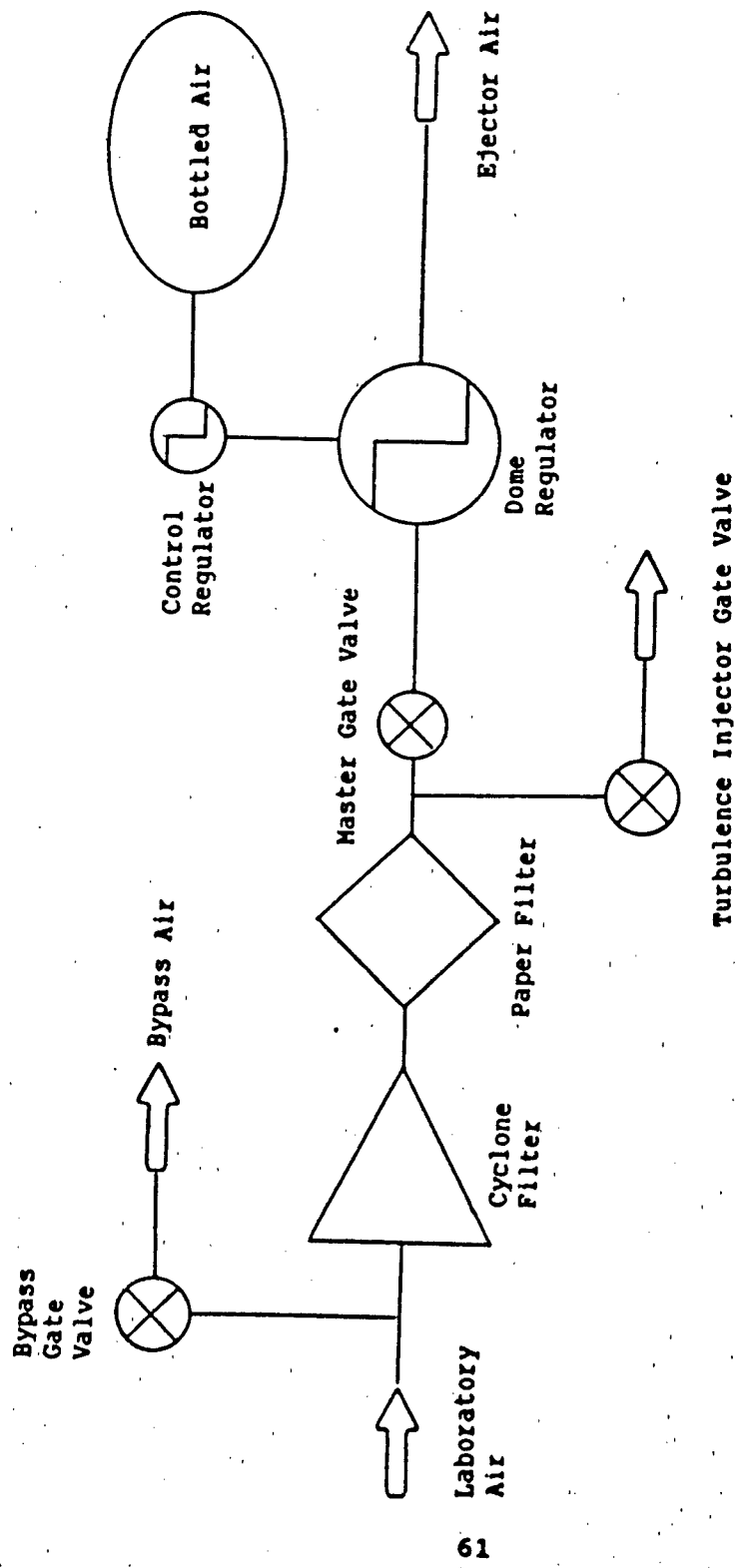
Figure 4. The AFIT Cascade Test Facility
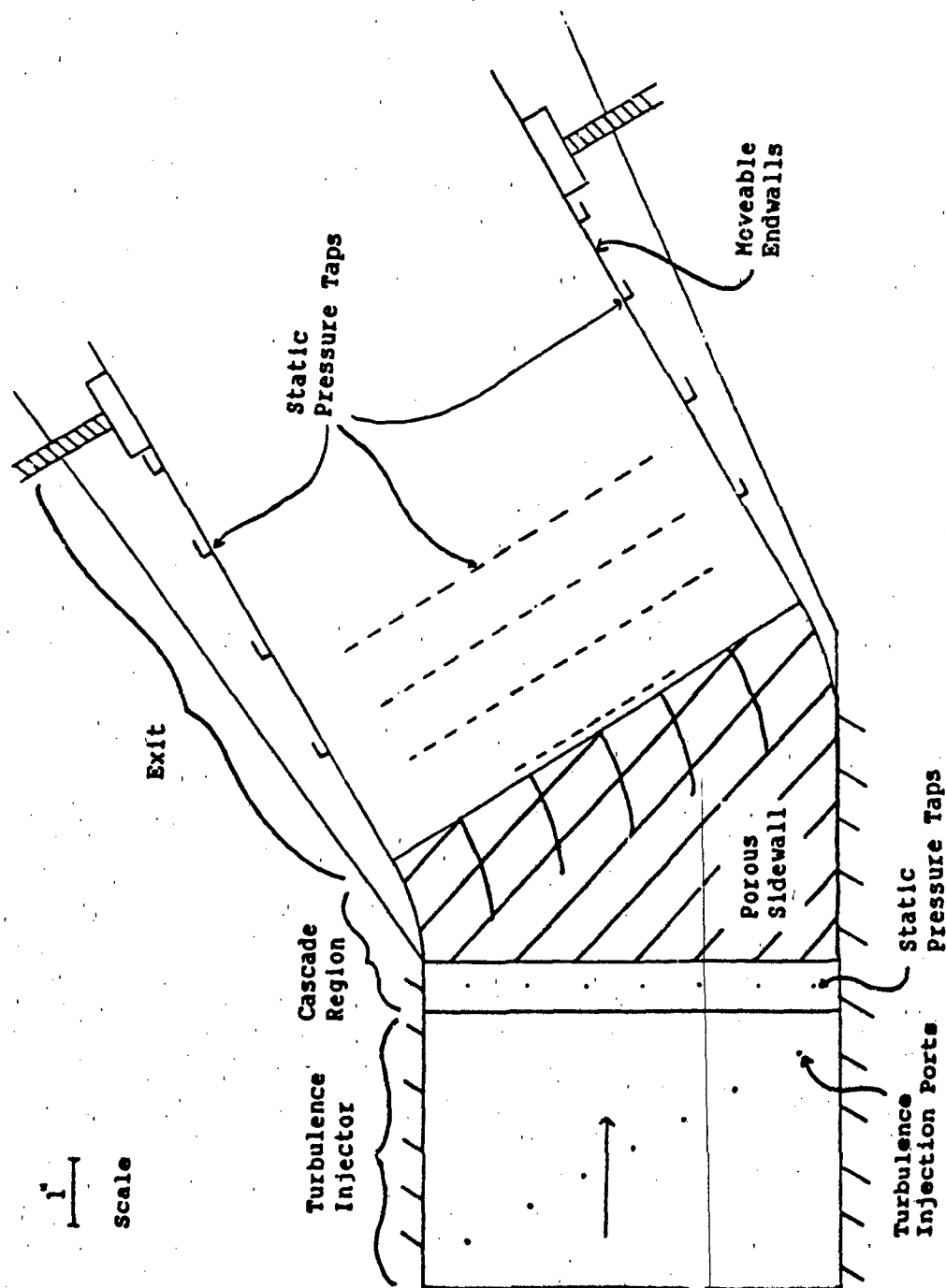
Figure 5. Schematic of the Ejector Supply System

Figure 6. Test Section

Static
Pressure Taps

Moveable
Endwalls

Exit

Static
Pressure Taps

Porous
Sidewall

Turbulence
Cascade
Injector
Region

Turbulence
Injection Ports

1'
Scale

62
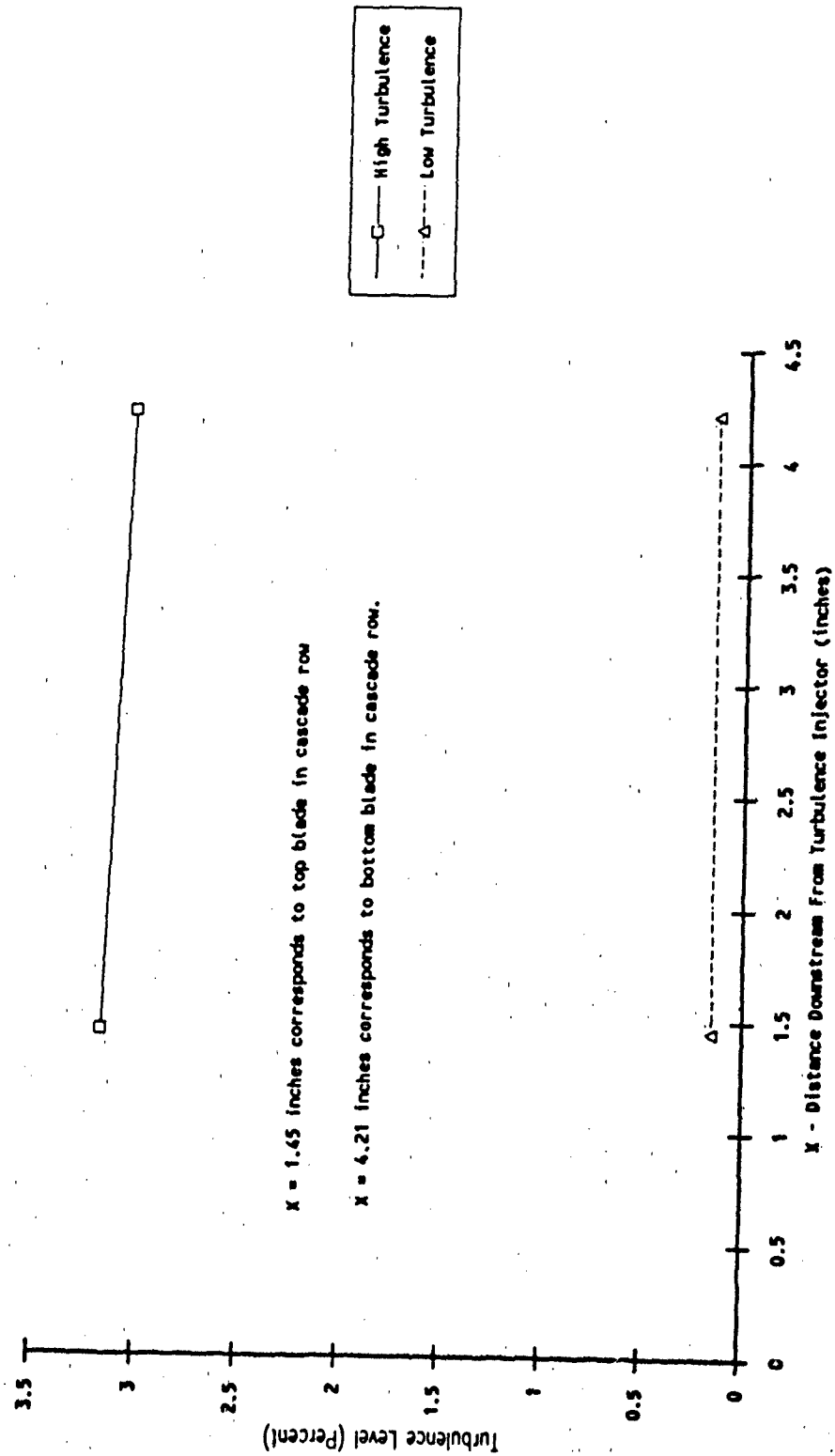
Figure 7. Turbulence Level Across Cascade — $Re_c \approx 430,000$

X = 1.45 inches corresponds to top blade in cascade row

X = 4.21 inches corresponds to bottom blade in cascade row.

High Turbulence
Low Turbulence

Turbulence Level (Percent)

X - Distance Downstream From Turbulence Injector (Inches)
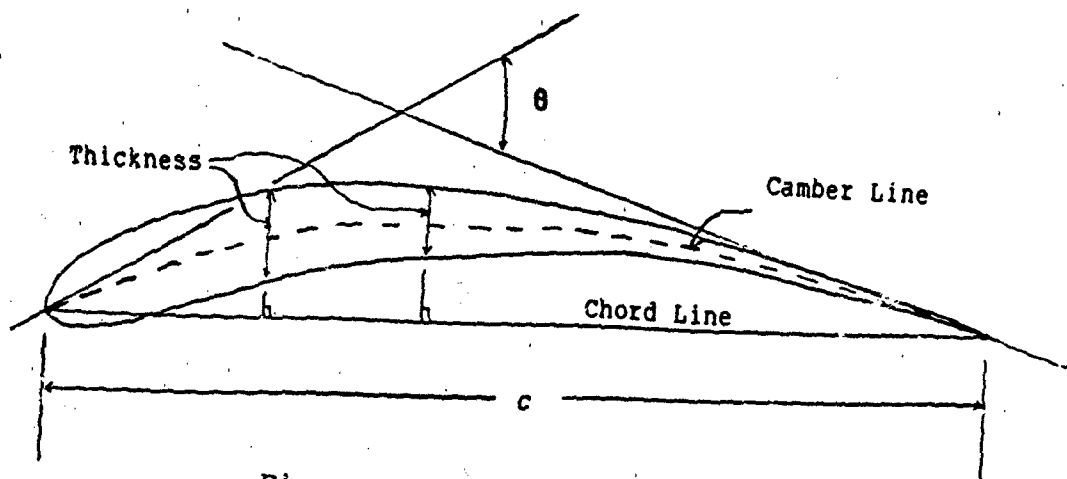
Figure 8. Airfoil Geometry
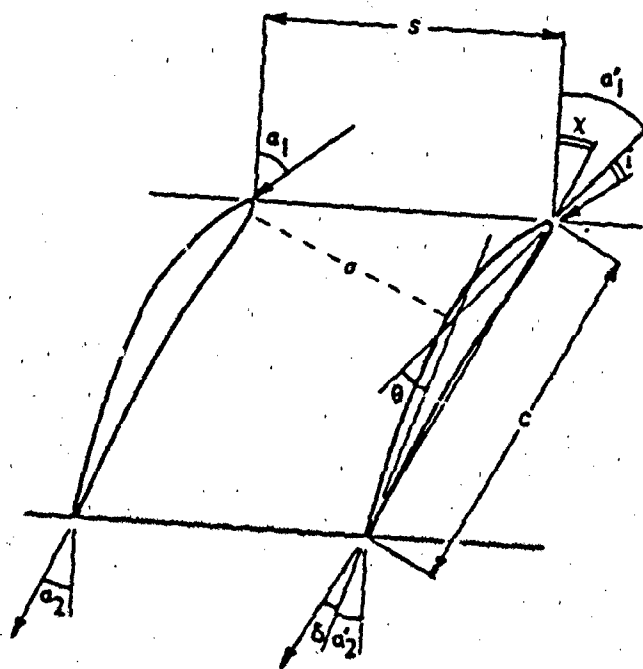
Figure 9. Cascade Geometry

64
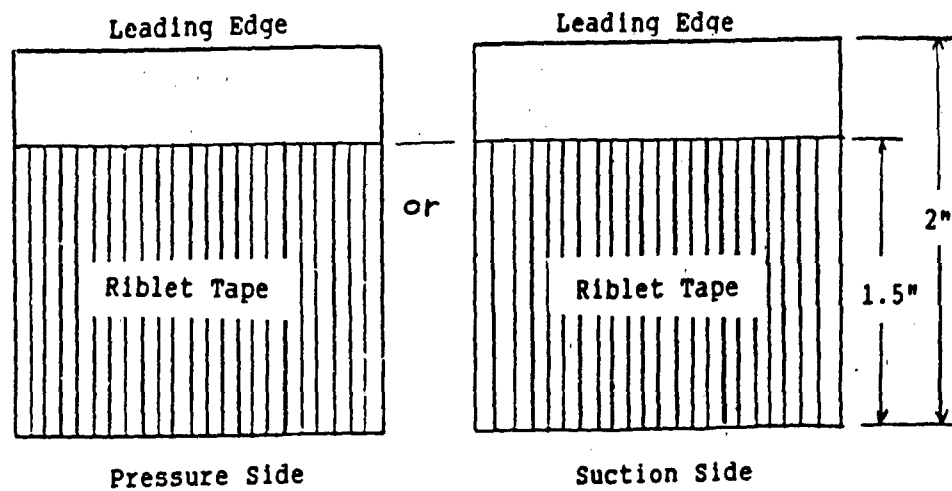
Figure 10. Placement of Riblets on Blades
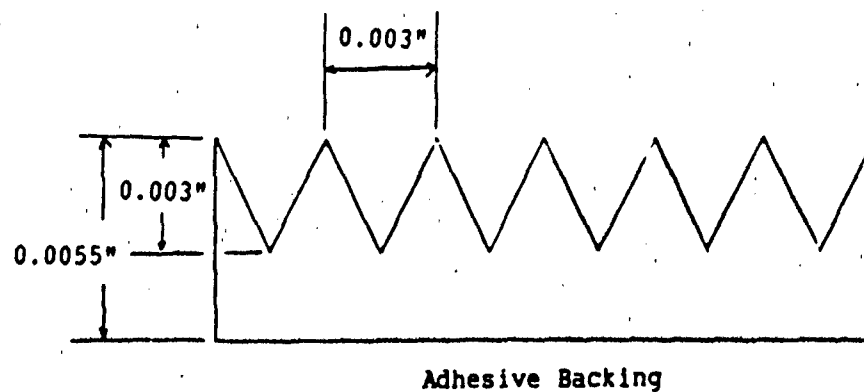
Figure 11. Riblet Geometry

65
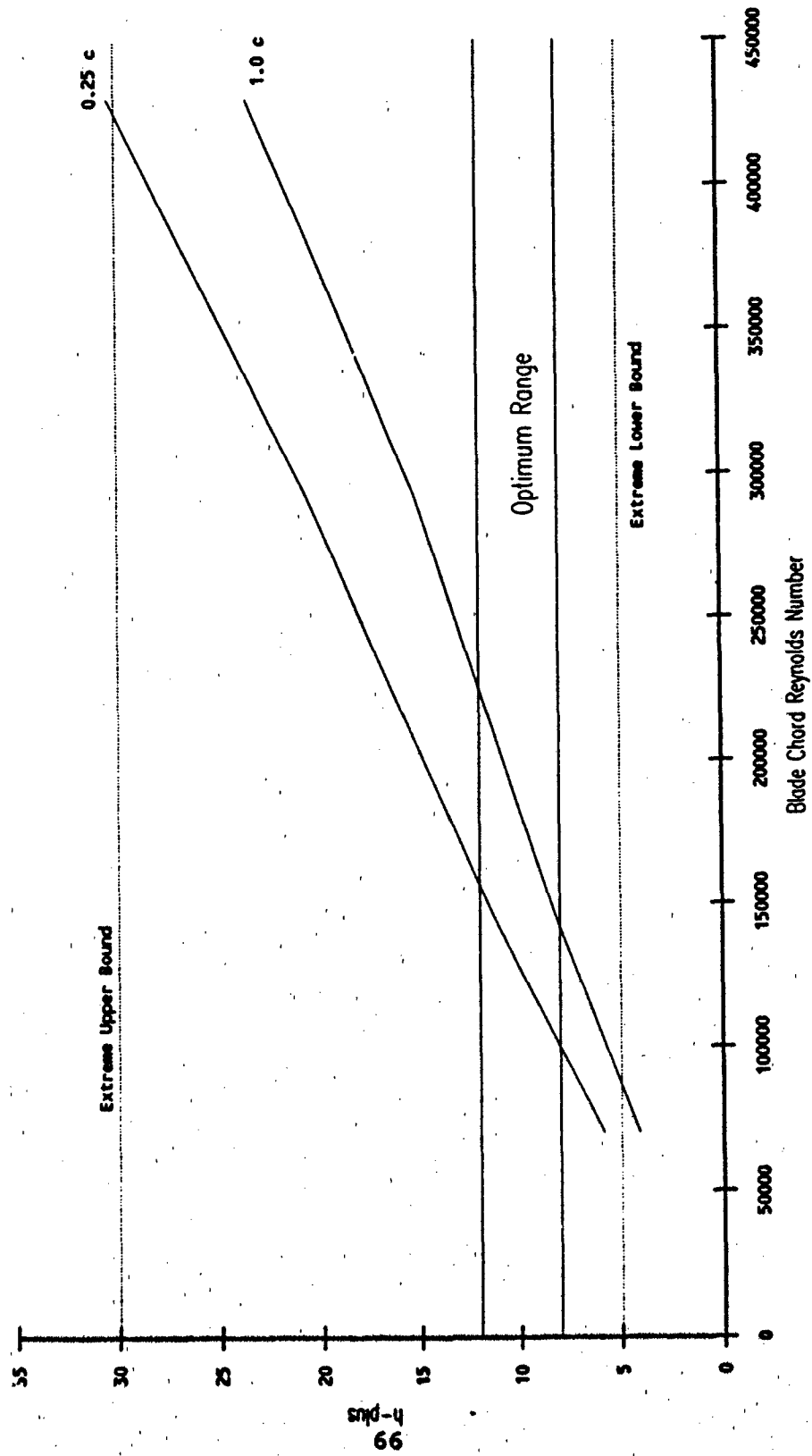
Figure 12. Estimation of h^+ vs Blade Chord Reynolds Number

Extreme Upper Bound

0.25 c

1.0 c

Optimum Range

Extreme Lower Bound

Blade Chord Reynolds Number

h-plus

66

0   50000   100000   150000   200000   250000   300000   350000   400000   450000

0   5   10   15   20   25   30   55

X-Mobility

Y-Mobility

Probe
Holder

Probe

Also Z-
Mobility

Support
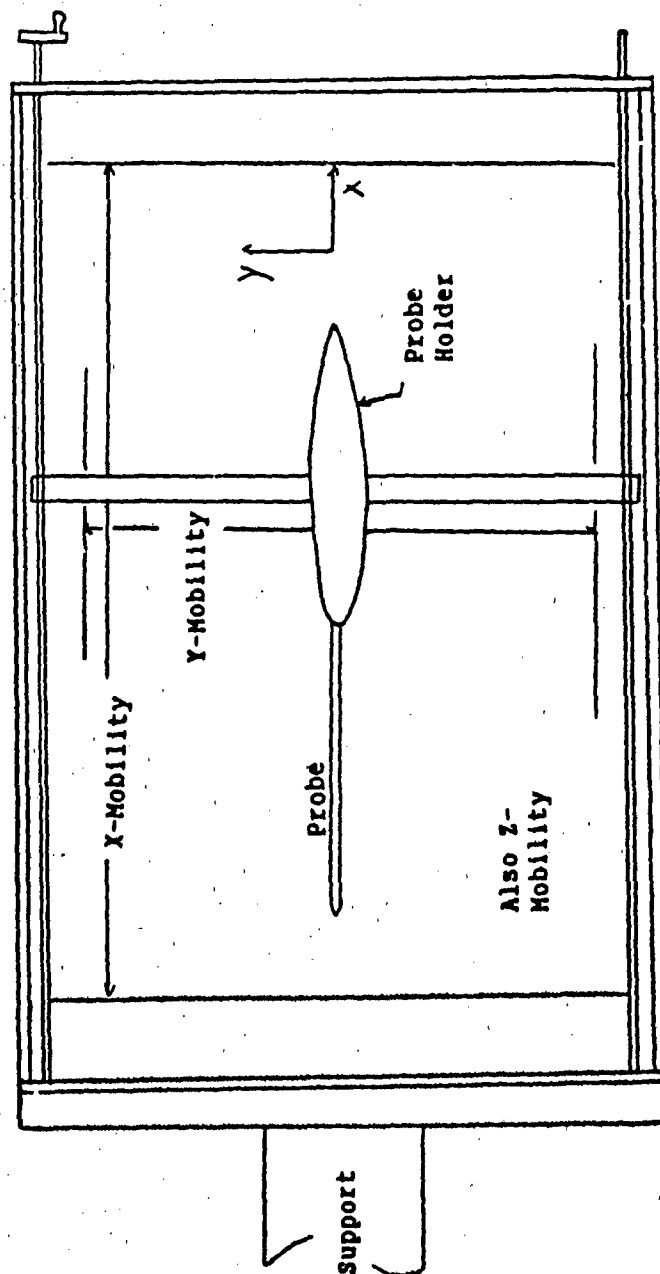
Figure 13. Traversing Mechanism

67
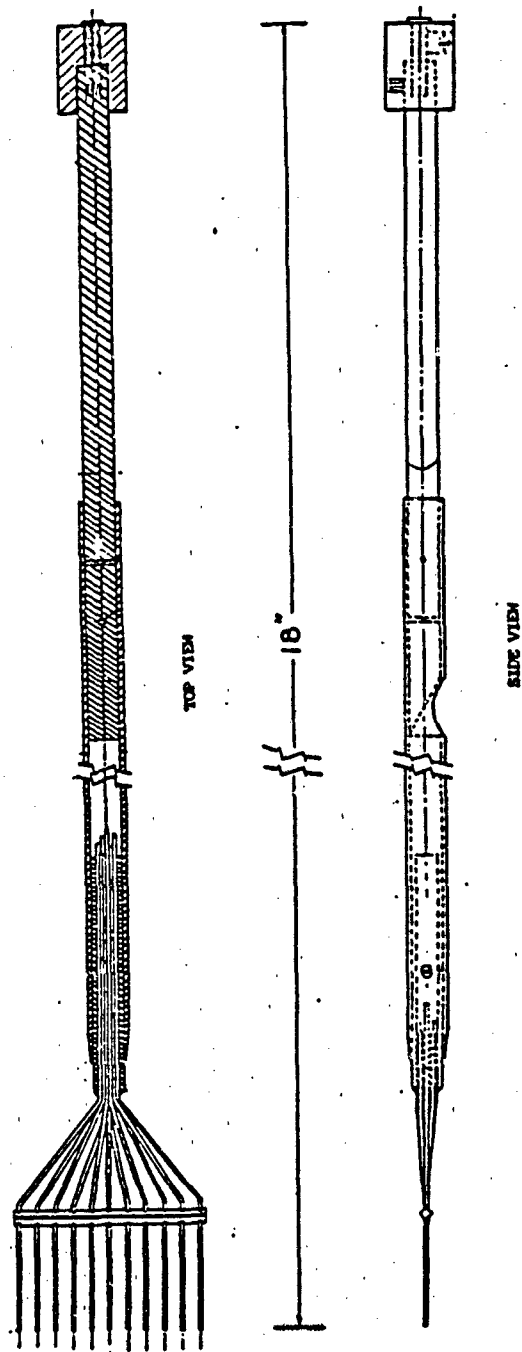
Figure 14.   Eleven Port Pressure Rake
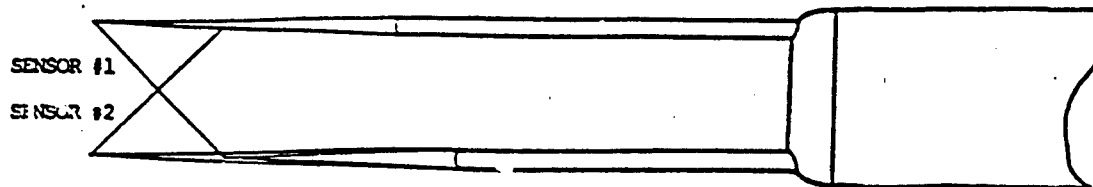
Figure 15.   Hot Film Probe Configuration
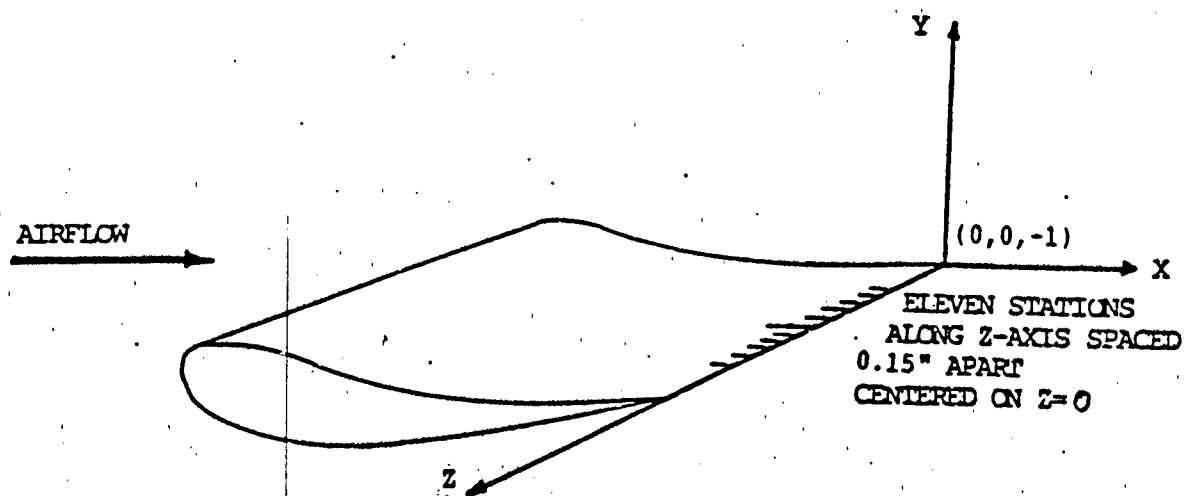
Figure 16.   Pressure Rake Data z Coordinates
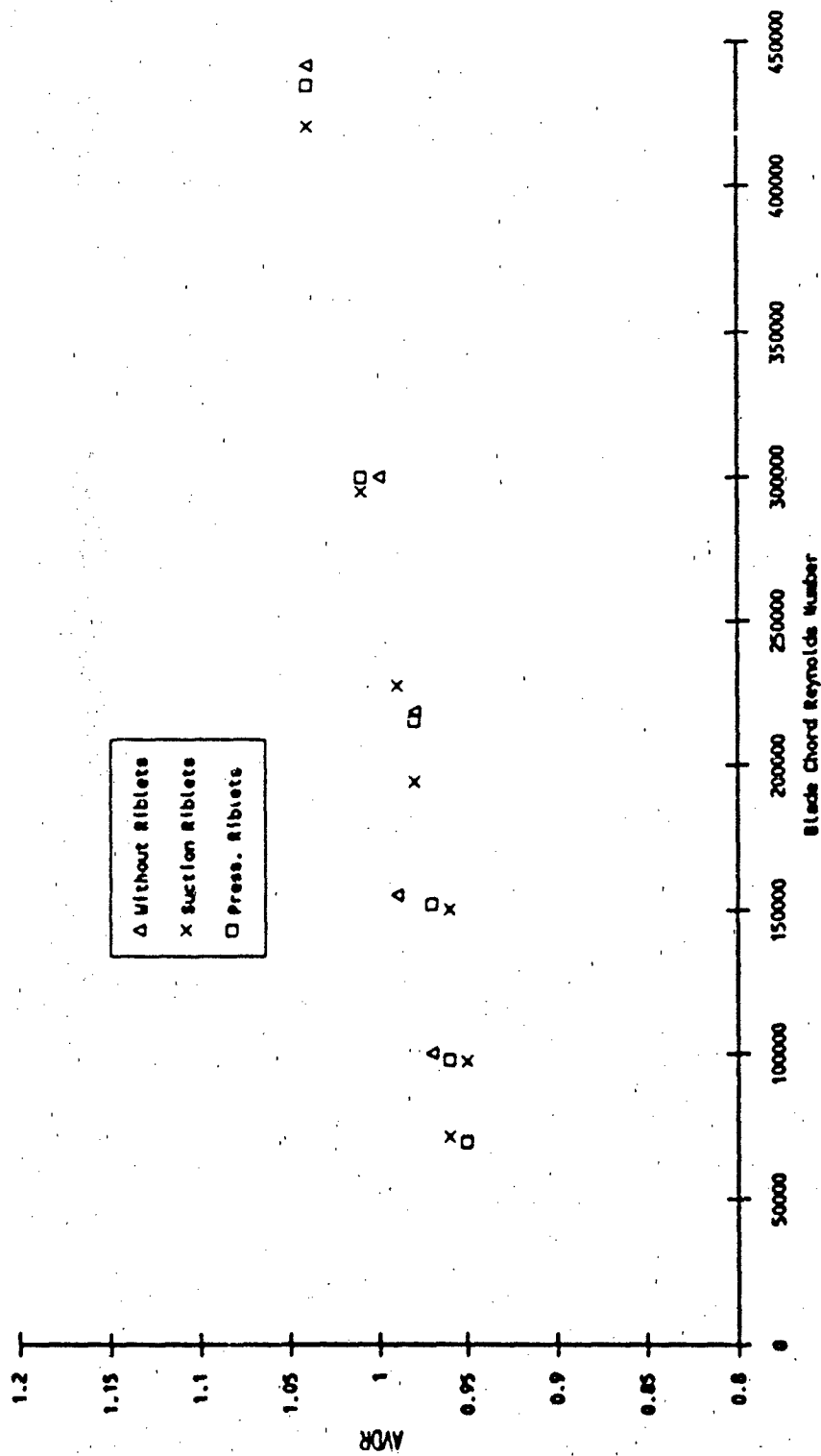
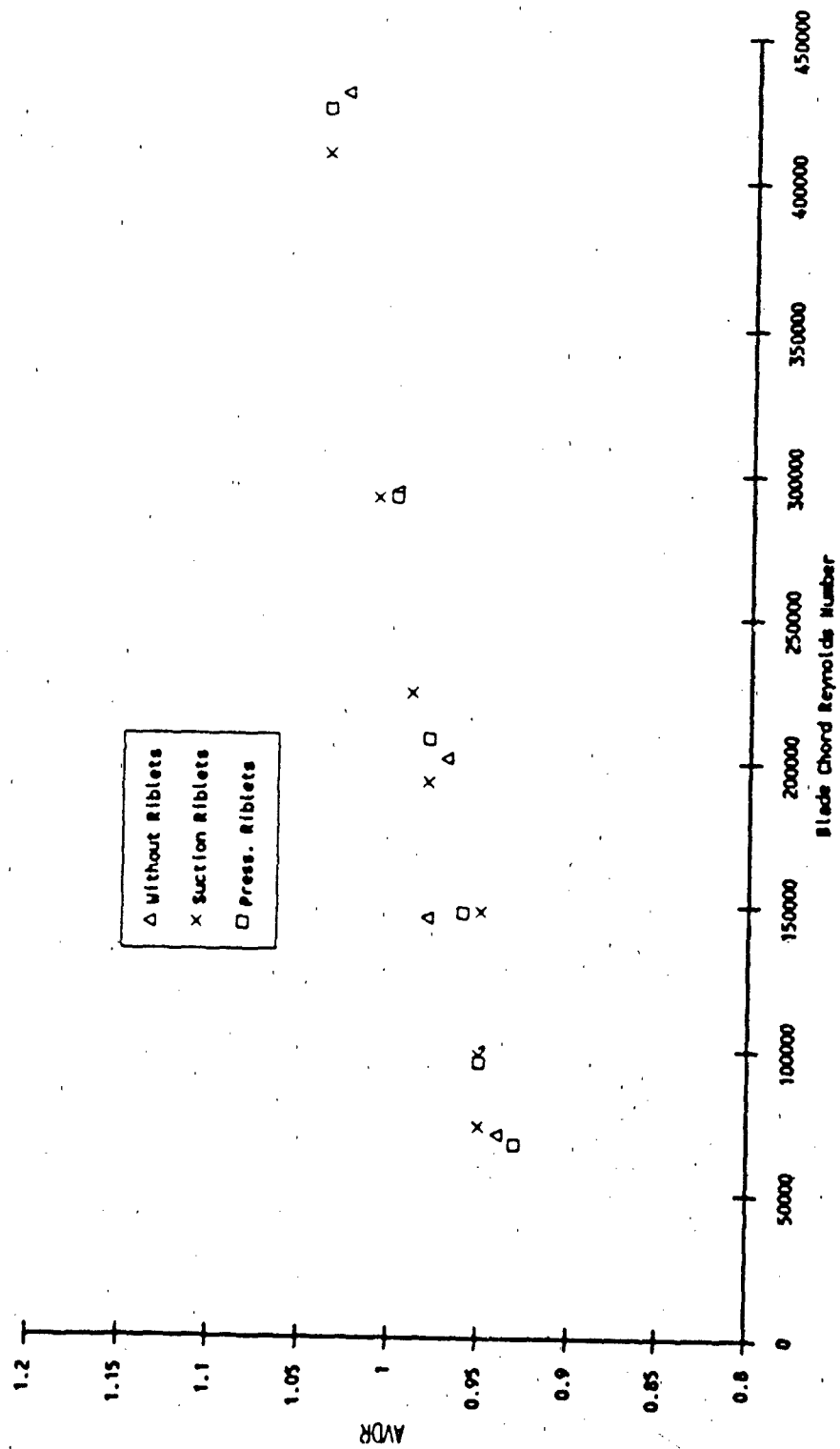Figure 17. AVDR vs Blade Chord Reynolds Number - Low Turbulence

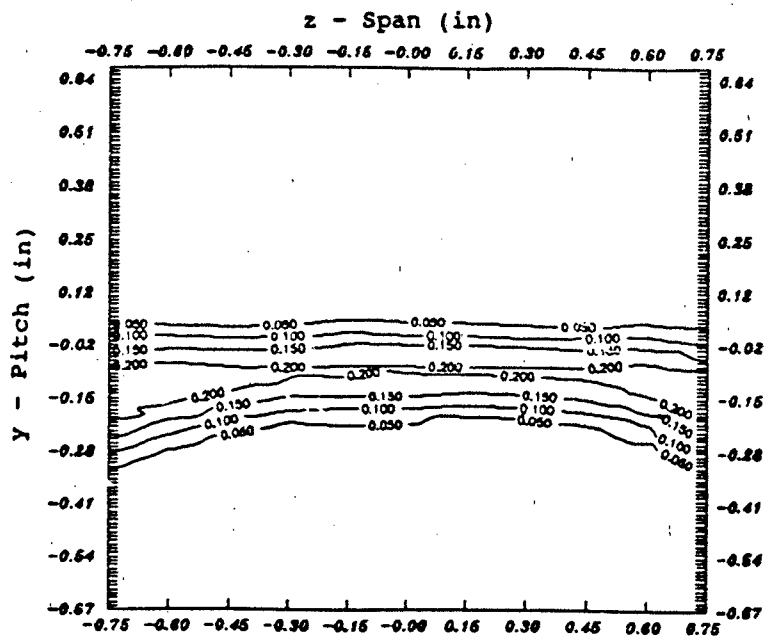Figure 18. AVDR vs Blade Chord Reynolds Number - High Turbulence
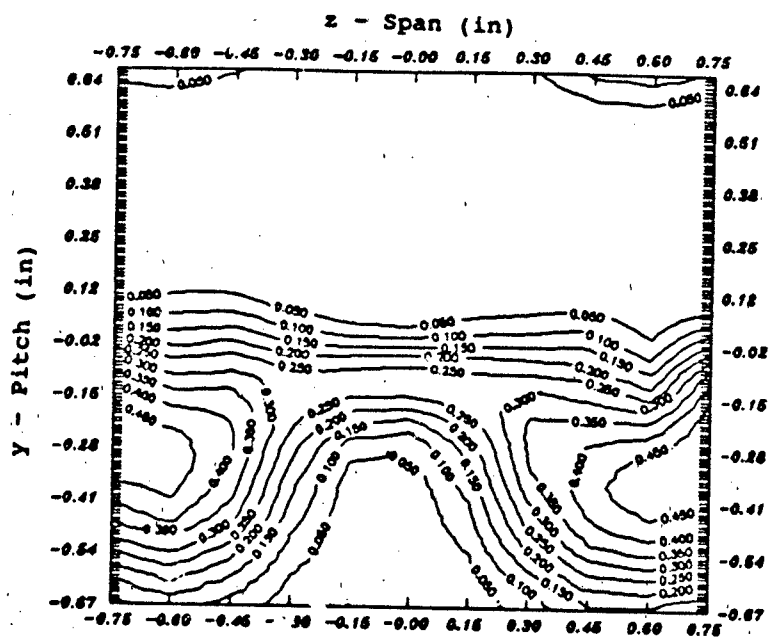
Figure 19.a.   Re = 70k, Low Turbulence, Set #1

Figure 19.b.   Re = 430k, Low Turbulence, Set #1

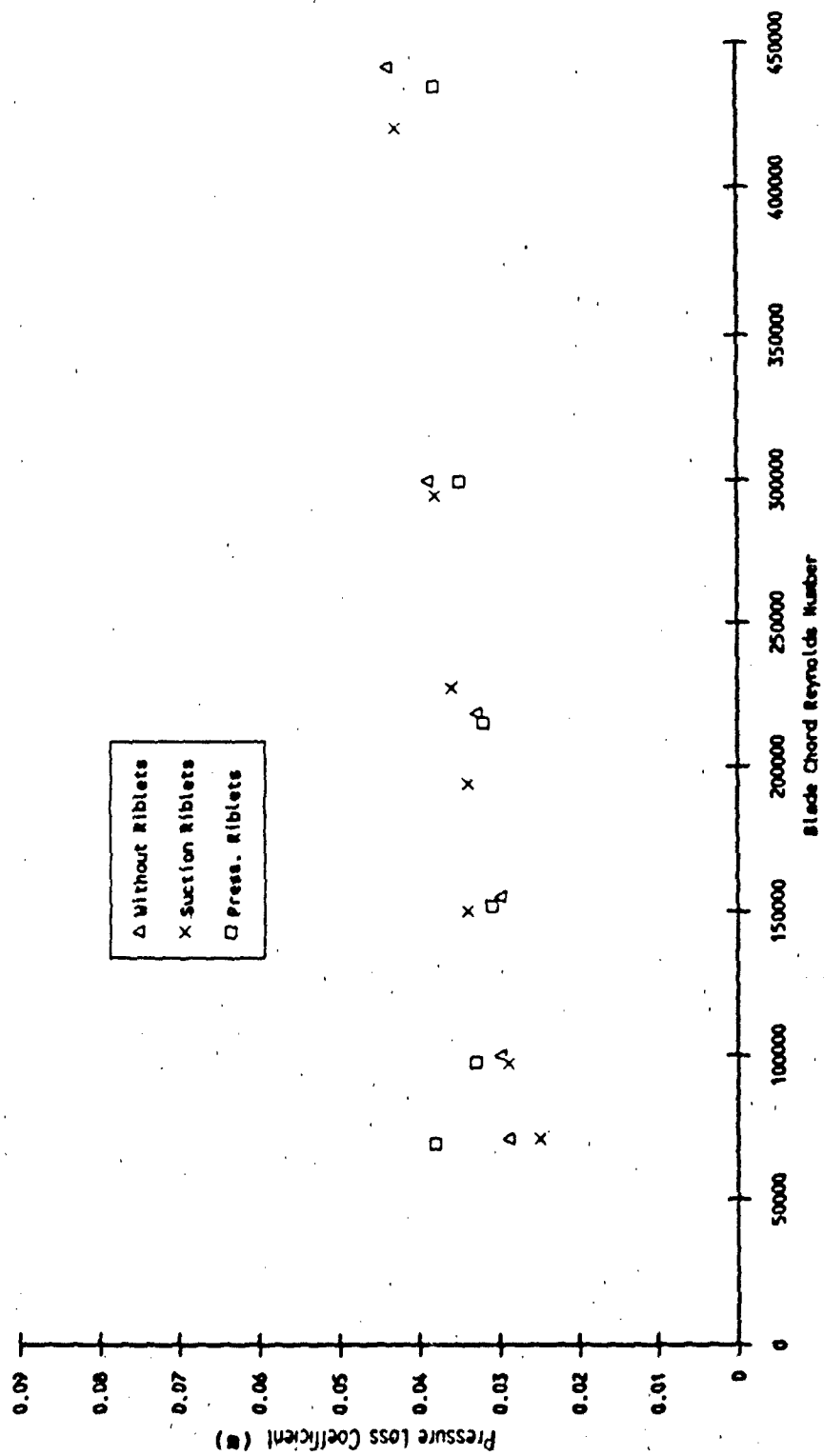Figure 19.   Total Pressure Loss Contours

Figure 20. Total Pressure Loss Coefficient vs Blade Chord Reynolds Number – Low Turbulence
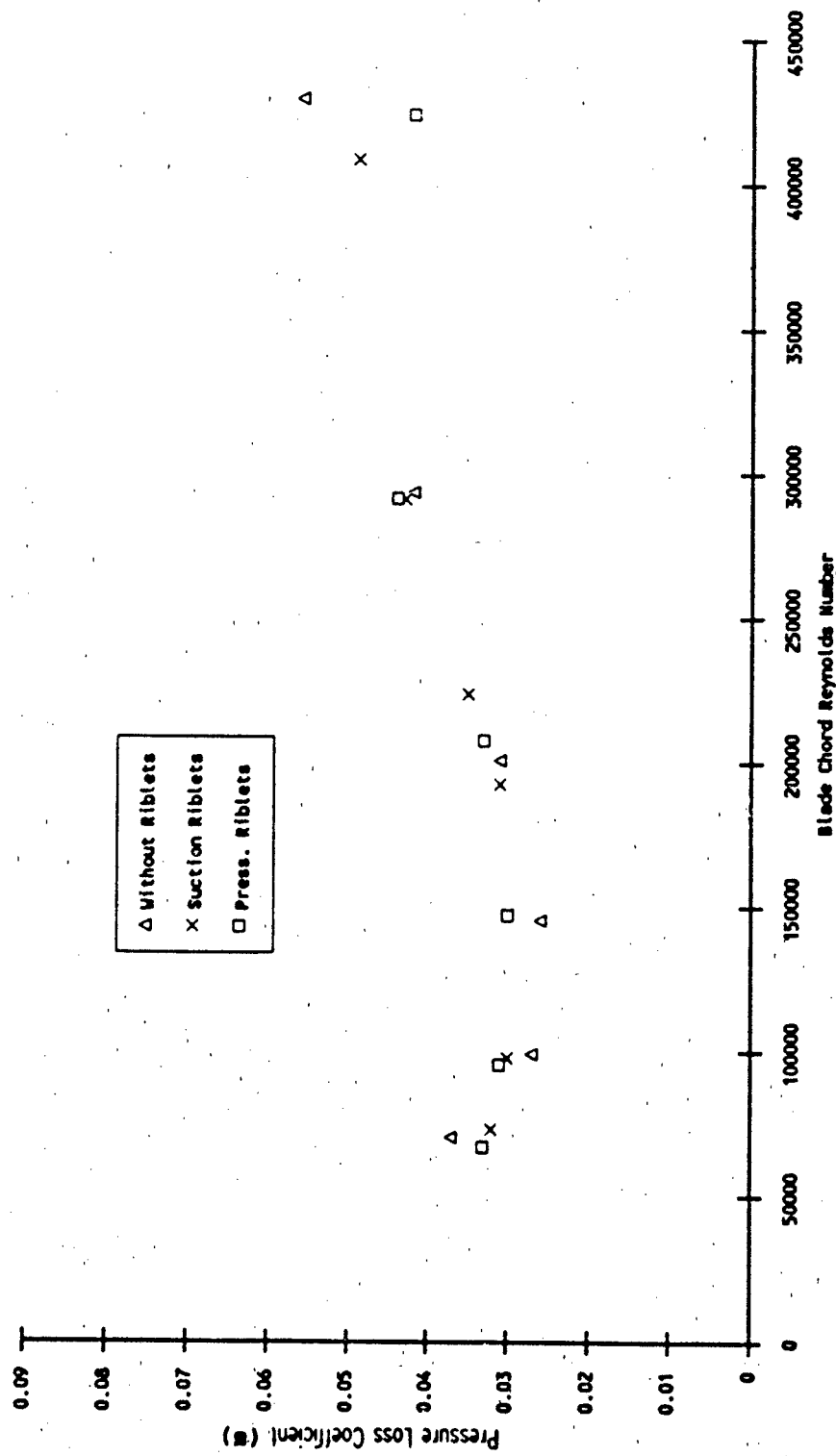
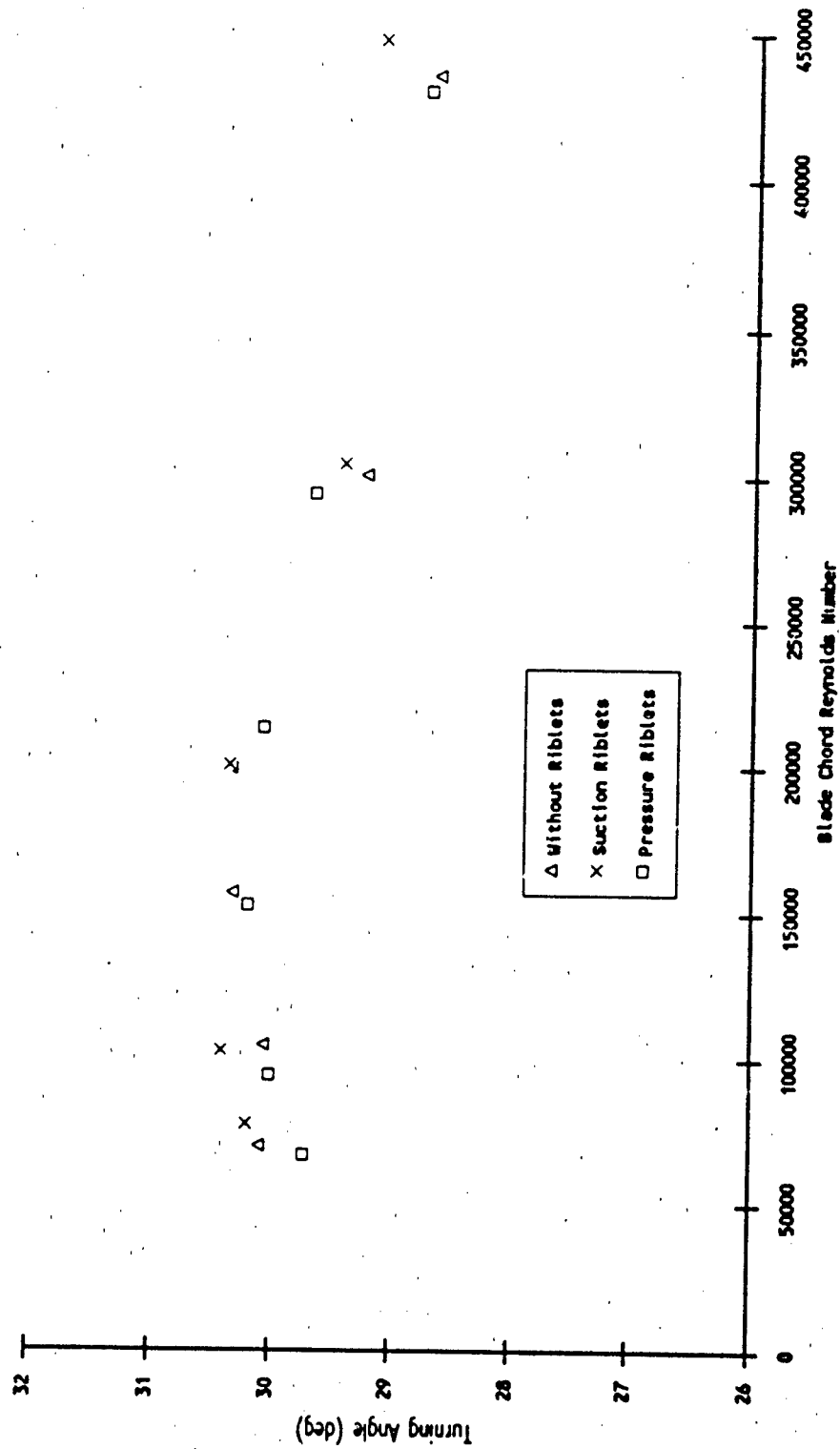Figure 21. Total Pressure Loss Coefficient vs Blade Chord Reynolds Number - High Turbulence

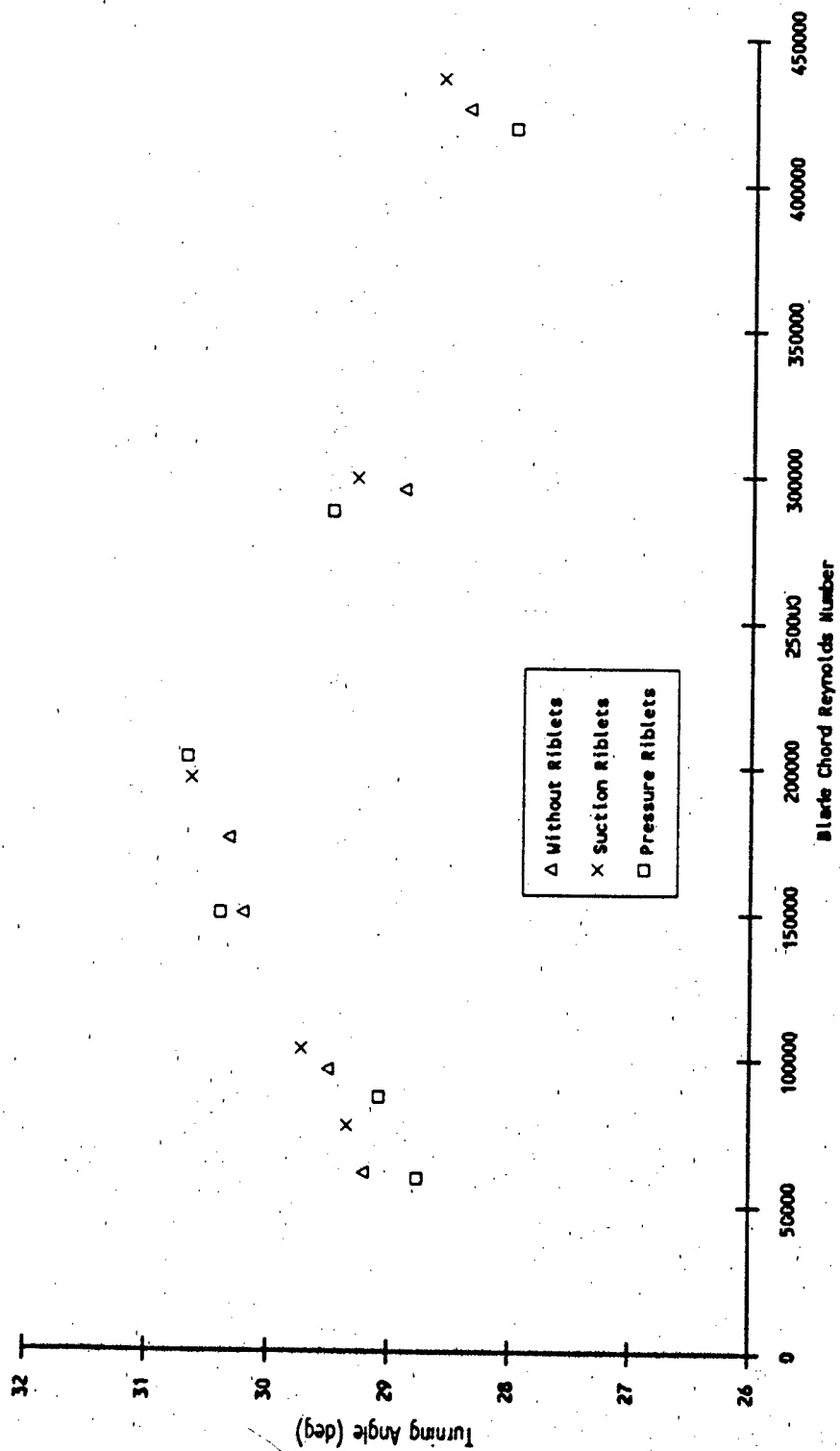Figure 22. Turning Angle vs Blade Chord Reynolds Number - Low Turbulence

75

Figure 23. Turning Angle vs Blade Chord Reynolds Number - High Turbulence

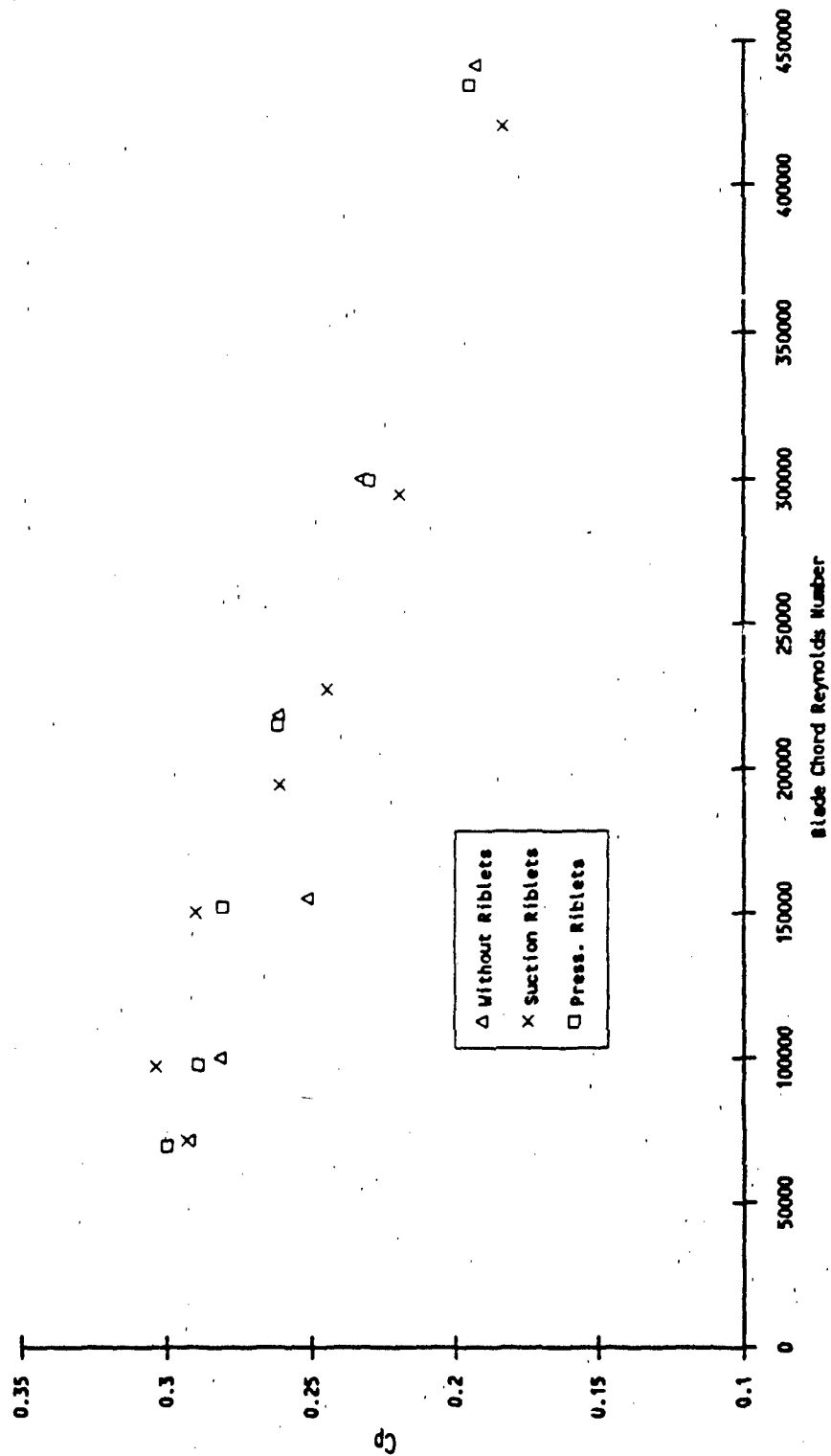Figure 24. Pressure Rise Coefficient vs Blade Chord Reynolds Number – Low Turbulence

77
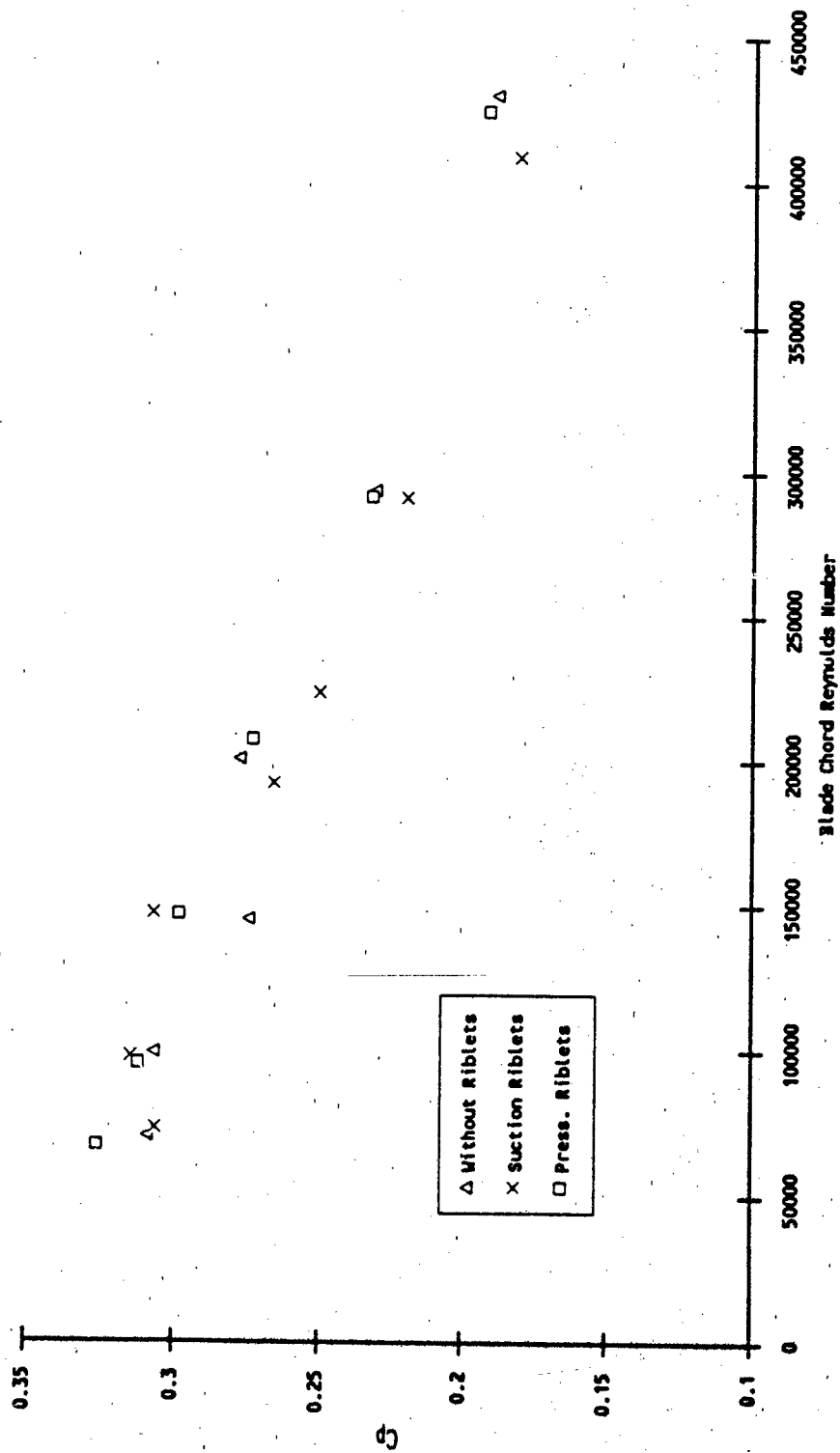
Figure 25. Pressure Rise Coefficient vs Blade Chord Reynolds Number - High Turbulence

Figure 26. Non-Dimensional Velocity Profile – Re_c = 70,000 – Low Turbulence

Figure 27.   Non-Dimensional Velocity Profile - Re$_c$ = 250,000 - Low Turbulence

Legend:
× Without Riblets
— Suction Riblets
+ Press. Riblets

Pitch (in)

Ve/Vin

80

Figure 28. Non-Dimensional Velocity Profile – $Re_c \approx 430,000$ – Low Turbulence

Figure 29. Non-Dimensional Velocity Profile – $Re_c \approx 70,000$ – High Turbulence

Figure 30. Non-Dimensional Velocity Profile - $Re_c \approx 250,000$ - High Turbulence
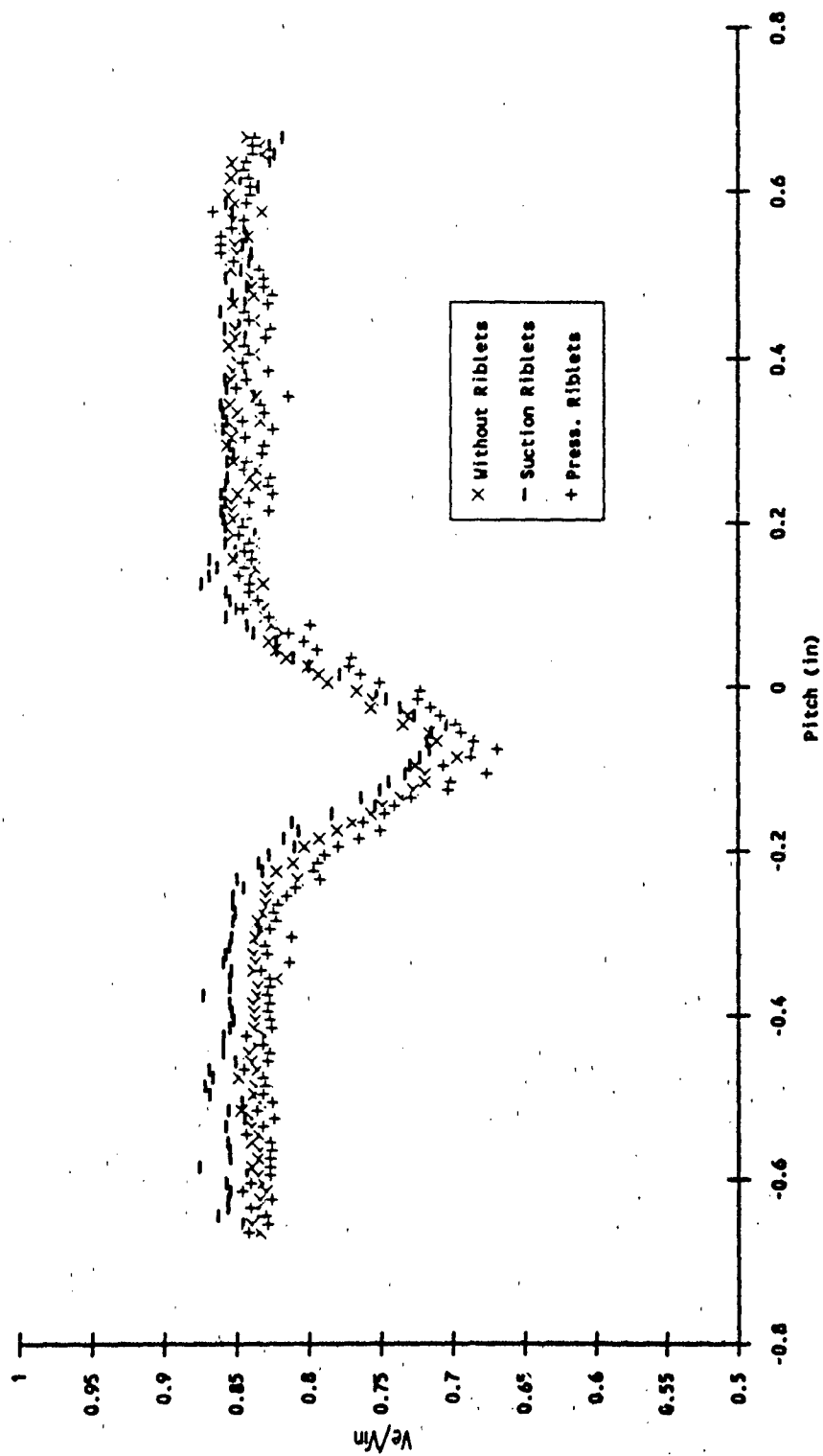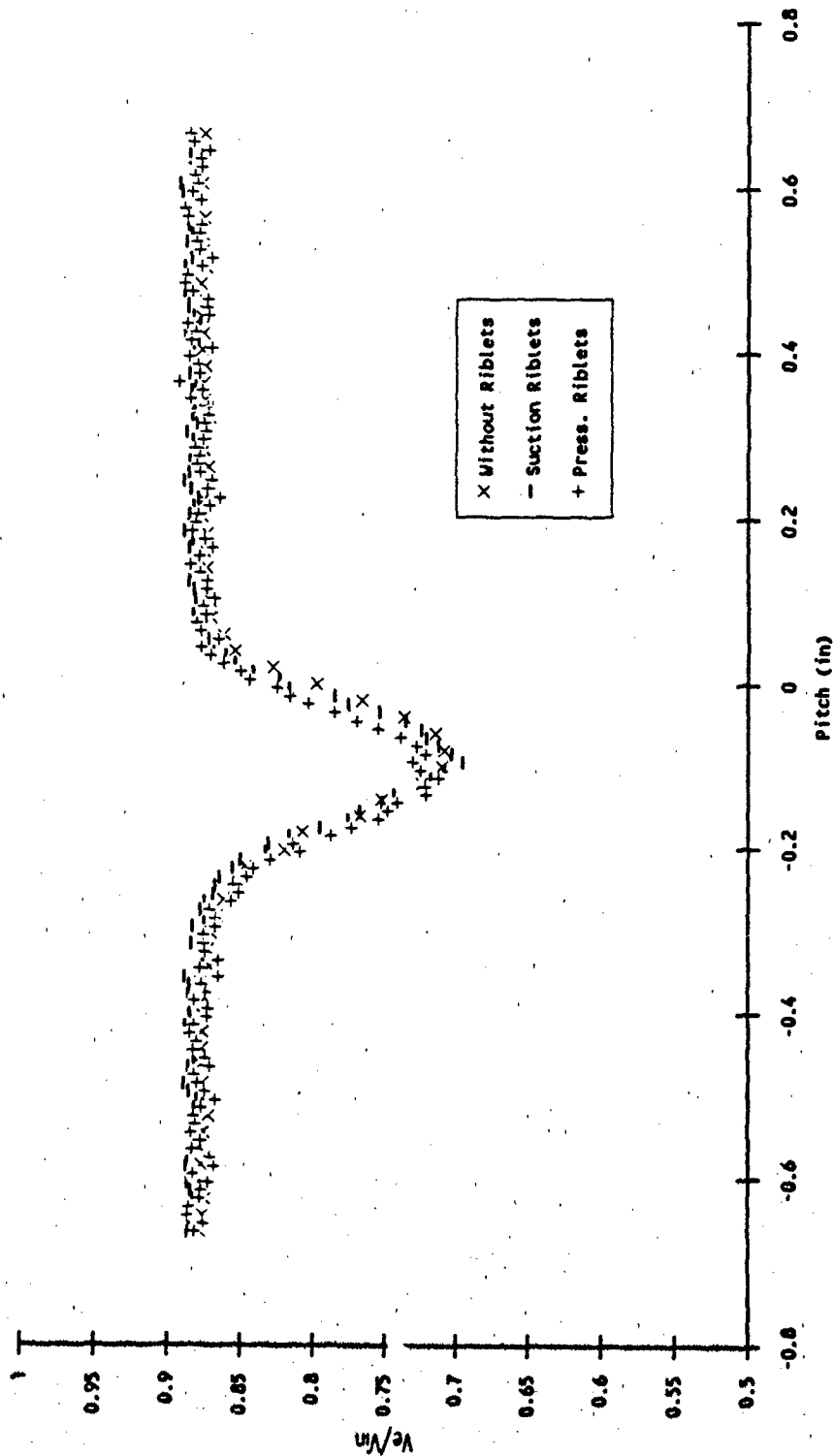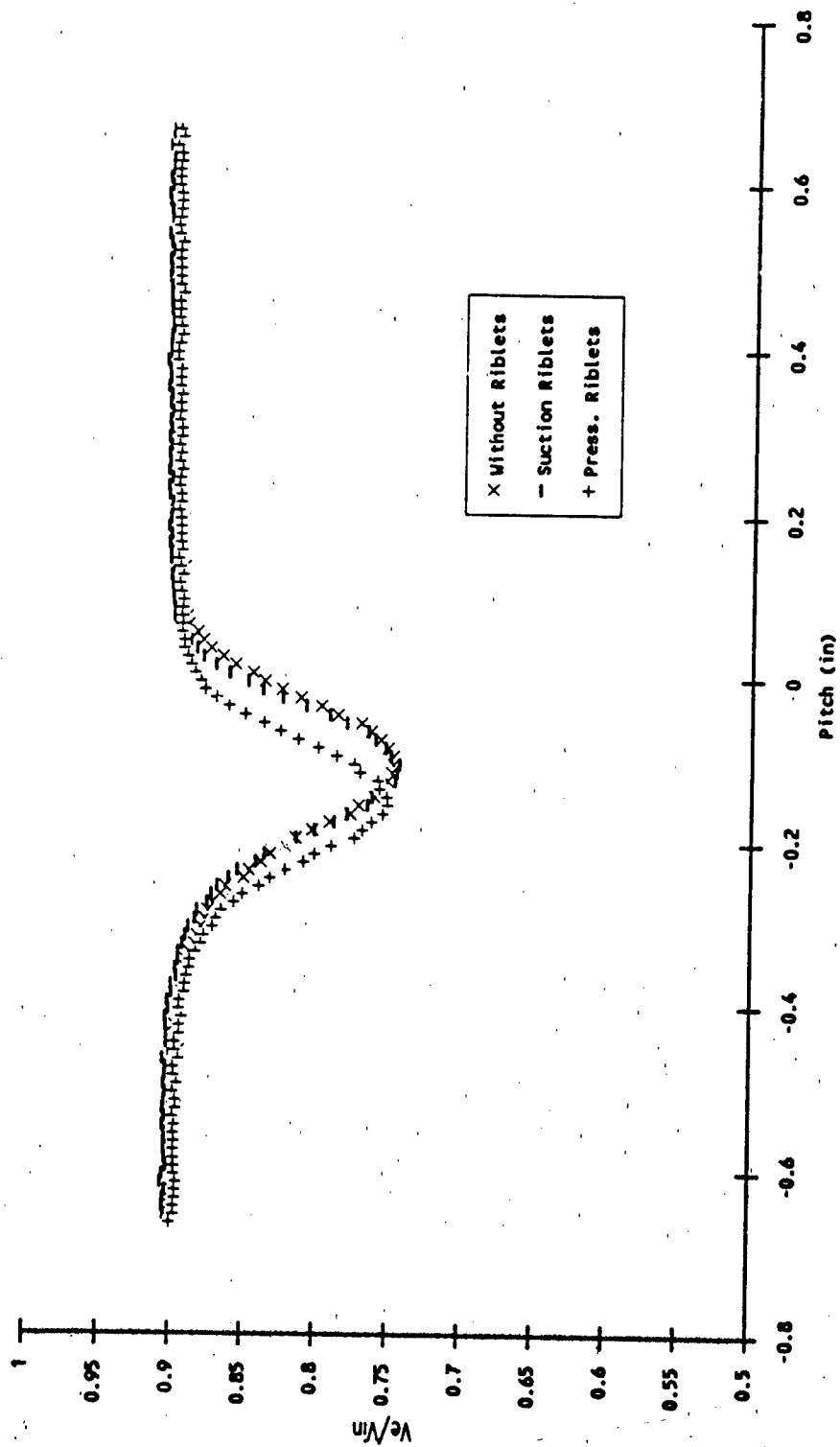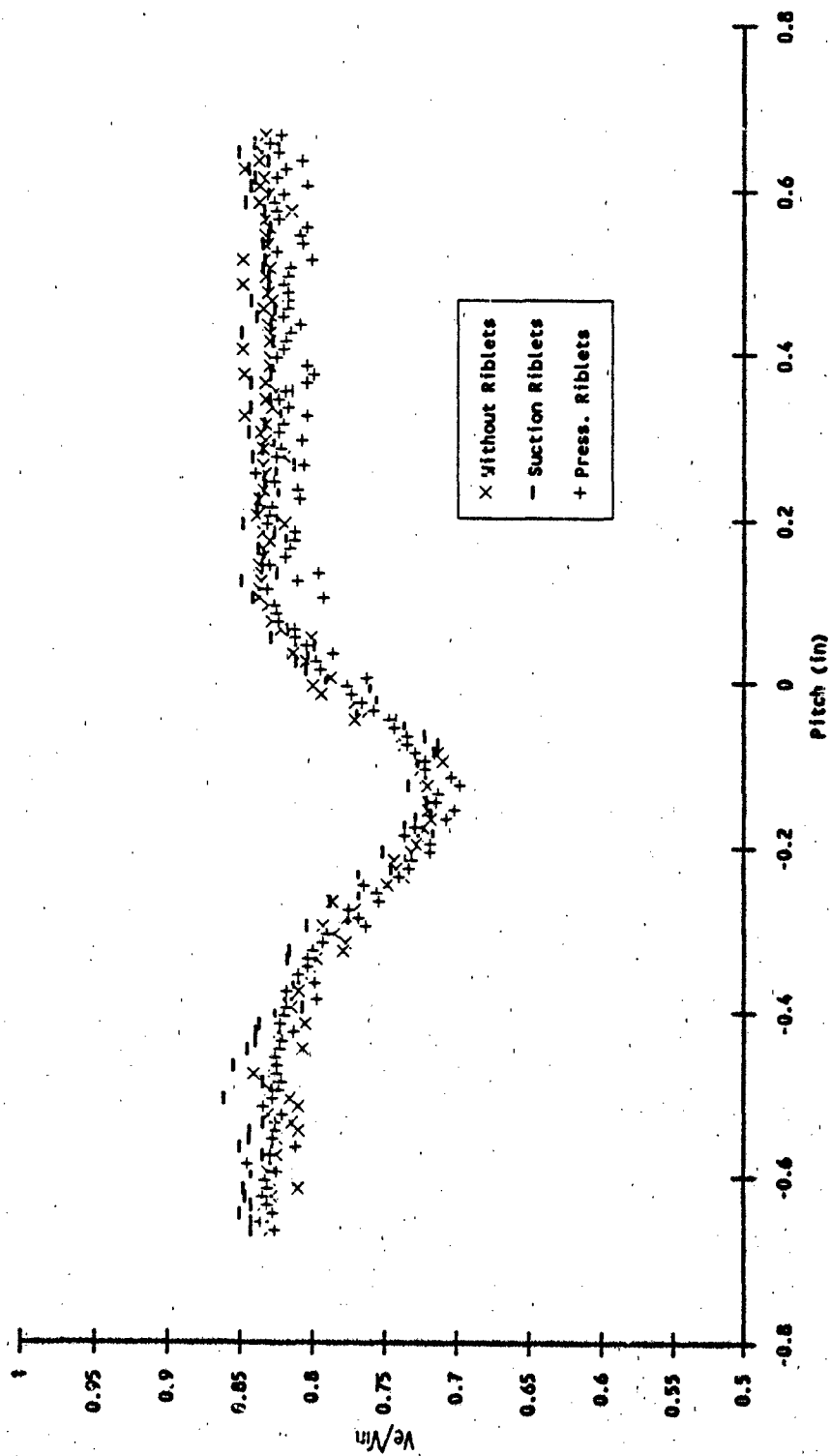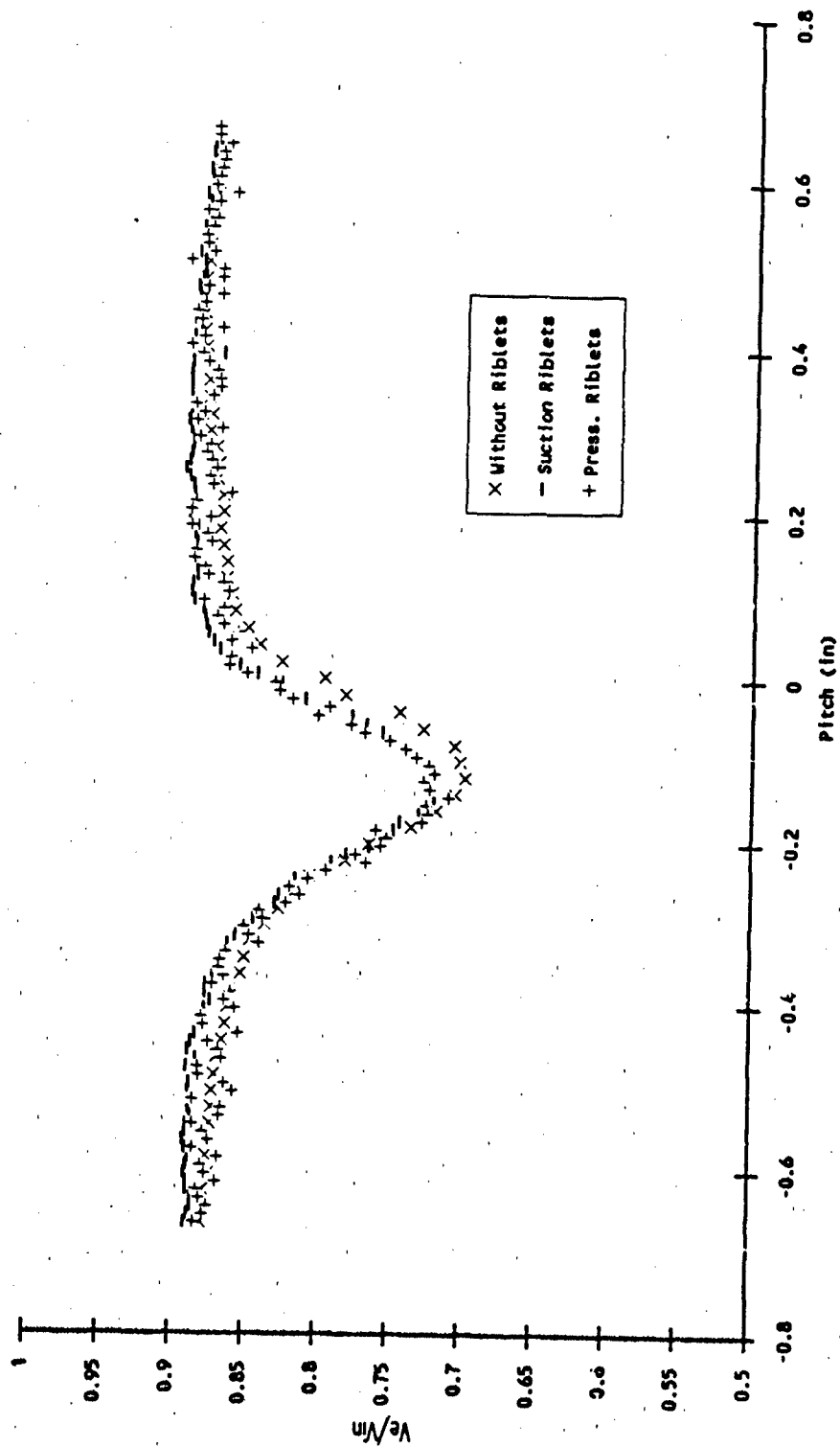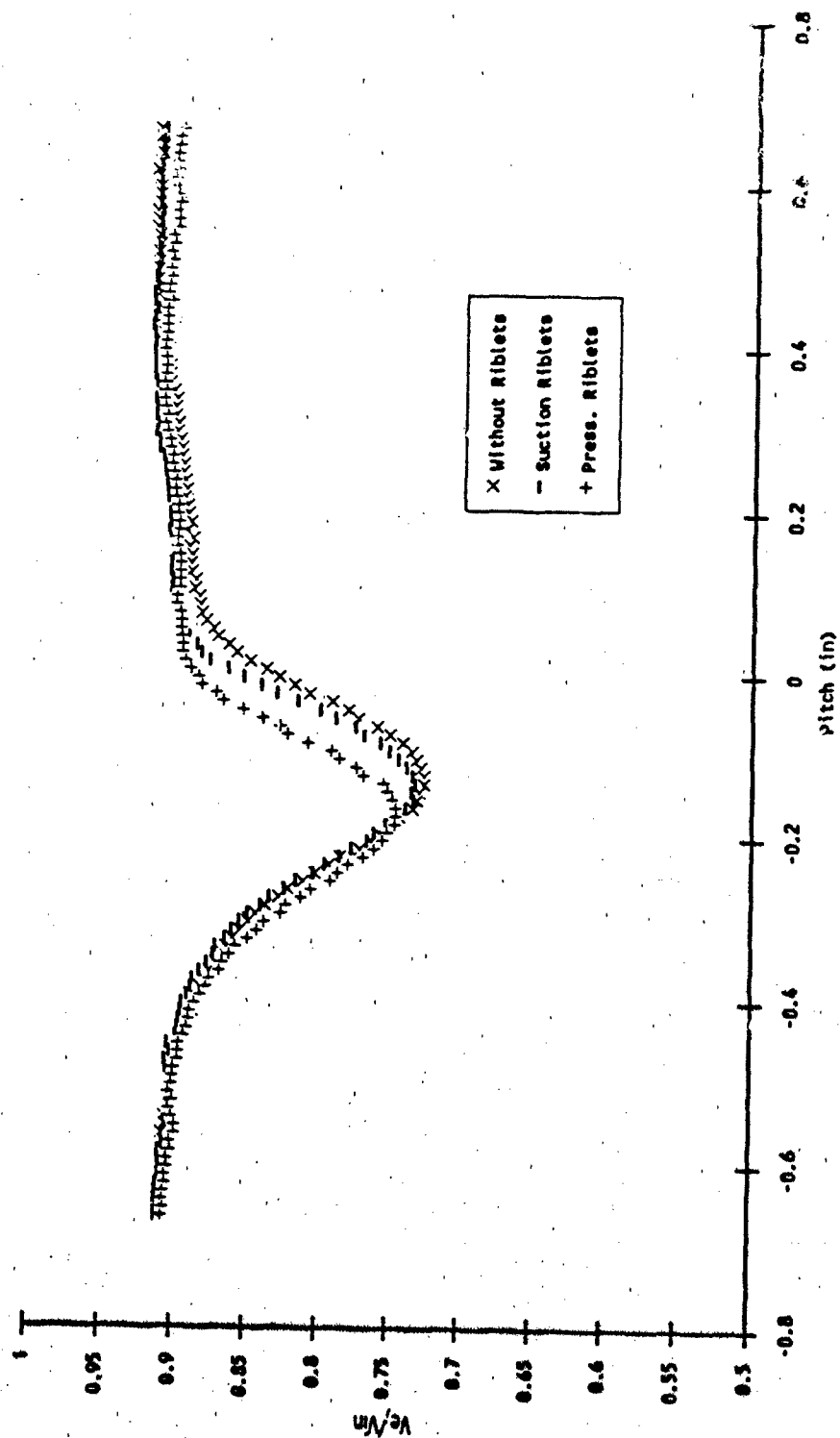
Figure 31. Non-Dimensional Velocity Profile – $Re_c = 430,000$ – High Turbulence

Appendix A. Component Listing.

Component	Model/Serial No.
Pressure Transducers	
Atmospheric/0-16 psia	CEC 4-326-0003/15666
Tank Total/±5 psig	Endevco 8510B-5/E25R
Throat Static/±2 psig	Statham PM60TC/4474
Exit Static/±2 psig	Statnam Labs PM60TC
Backup/±2 psig	Statham Labs PM60TC
Balancing/±2.5 psig	Scanivalve/SS2 48
Film Calibrator/±5 psig	Endevco 8510B-5/90EK
P-Rake #1/±0.5 psig	Statham PM96TC/3833
#2/±1.0 psig	Statham P96/1459
#3/±0.5 psig	Statham PM96TC/3818
#4/±0.5 psig	Statham PM96TC/3819
#5/±0.5 psig	Statham PM96TC/3838
#6/±1.0 psig	Statham P96/1476
#7/±1.0 psig	Statham P95/1471
#8/±0.5 psig	Statham PM96TC/3831
#9/±1.0 psig	Statham PM96TC/3788
#10/±0.5 psig	Statham PM96TC/3823
#11/±0.5 psig	Statham PM96TC/3836
Scanivalve System	
Pressure Transducer	PDCR 23D
Scanivalve	48S9-3003
Position Display	J102/J104
Thermoccuples	
Copper Constantan (4)	Omega T-type
Ambient	
Tank Total	
Calibrator Top	
Calibrator Bottom	
Traversing Mechanism	
Motors (2)	NEAT 310
X-Encoder	Astrosystems/8131
Vacuum System	Shop Vac Industrial duty Model 984/3.5 hp

Hot Film Anemometer System

Anemometer	TSI IFA 100
Voltmeter	TSI IFA 200
X-configuration Hot Film	TSI Model 1241-10
X-configuration Probe Support	TSI Model 1155-18
Calibrator (modified)	TSI Model 1125

Central Computer   Zenith Model Z-248

Appendix B.   Pressure Transducer Calibration.

Prior to calibration, all pressure transducers were exercised through their entire range of operation.   Each transducer was then subject to an 11 or 21 point bi-directional calibration which spanned the expected range of operation of the transducer during data acquisition.   The pressures were supplied by a dead weight tester, and the pressure was monitored directly at the transducer by a vertical, U-tube water manometer.

All pressure transducer calibration curves were linear and well behaved.   The statistical correlation calculated for the calibration data of each transducer is given in the following table:

Table 2.   Transducer Correlations

Transducer Number	Function	Correlation
1	ambient	1.00000
2	stilling tank	1.00000
3	throat static	0.99994
4	exit static	0.99998
5	backup	0.99991
6	Scanivalve	1.00000
7	HW calibrator	1.00000
8-17	rake #1-10	0.99999
18	rake #11	1.00000

Appendix C.   Hot Film Calibration.

If a body is placed in an air flow of different
temperature, heat transfer will result. If the air flow is
cooler than the body, heat will be transferred from the
body. According to basic thermodynamic principles, heat
transfer can take place three different ways: radiation,
conduction, and convection. In the case of hot film
anemometry, radiation and conduction are negligible. There
remain two possible types of convection: free convection,
and forced convection. In flows of sufficient velocity,
only forced convection need be considered. Such is the
case for this work.

The amount of heat transfer from a hot body to a
"cool" flow is directly proportional to the velocity of the
flow. Hot film and hot wire anemometry take advantage of
this fact by measuring how much energy is transferred from
an electrically heated wire to a flow of known temperature.
The rate of electrical energy input to the wire can be
equated to the relationship for convective heat transfer
rate as follows:

$$I_s^2 R_s = h_f A (T_s - T_f) \qquad (10)$$

The subscript "s" represents sensor values and the
subscript "f" represents fluid values. "I" and "R"

symbolizes the convection coefficient of the fluid. "A" is the exposed area of the body.

The current through a resistor is given by the voltage across the resistor divided by its resistance. In tne case of a metal wire, or film sensor in this case, the resistance can be maintained at a constant value by maintaining a constant te·iperature in the sensor. Assuming this resistance is known, and also assuming that the required voltage across the sensor can be measured, all terms on the left hand side of the above equation are known. It now remains to express the right hand side of the above equation in terms of the desired variable, velocity.

Since the sensor diameter and length are more likely to be known than its area, "A" can be substituted with $\pi d_s l_s$. The value h_f can be expressed in terms of Nusselt number via the following relationship:

$$h_f = \frac{Nu k_f}{d_s} \tag{11}$$

where k_f is the fluid conductive heat transfer coefficient. The Nusselt number and Reynolds number are related to each other quadratically, and a three term calibration

relationship employed, such as

$$Nu = A + B\sqrt{Re} + CRe \qquad (12)$$

where A, B and C are determined statistically. Since Re = $\rho V d_s / \mu$, all terms on the right hand side of equation (1) are now know, except for the velocity. Making the above substitutions, and keeping the right hand side of equation (1) in terms of the Nusselt number for now, the equation now becomes

$$\left(\frac{V_s}{R_s}\right)^2 R_s = \left(\frac{Nu k_f}{d_s}\right)(\pi d_s l_s)(T_s - T_f). \qquad (13)$$

In order to maintain the temperature of the sensor and still be able to accurately measure the voltage across it, the sensor is placed across one leg of a Wheatstone Bridge as illustrated in Figure 32. The total resistance of the of the sensor leg of the bridge (R_s) is the sum of the film (wire) resistance, R_w, the internal probe resistance, R_{pi}, the probe support resistance, R_{ps}, and the cable resistance between the probe and the bridge, R_c. R_{misc} in Figure 32 is equal to the sum of R_{pi}, R_{ps}, and R_c. The total resistance of the side of the bridge that contains the sensor is the sum of the sensor resistance, R_s, and the upper arm resistance, R_u. As the temperature of the sensor changes due to changes in the flow velocity or temperature, the

90
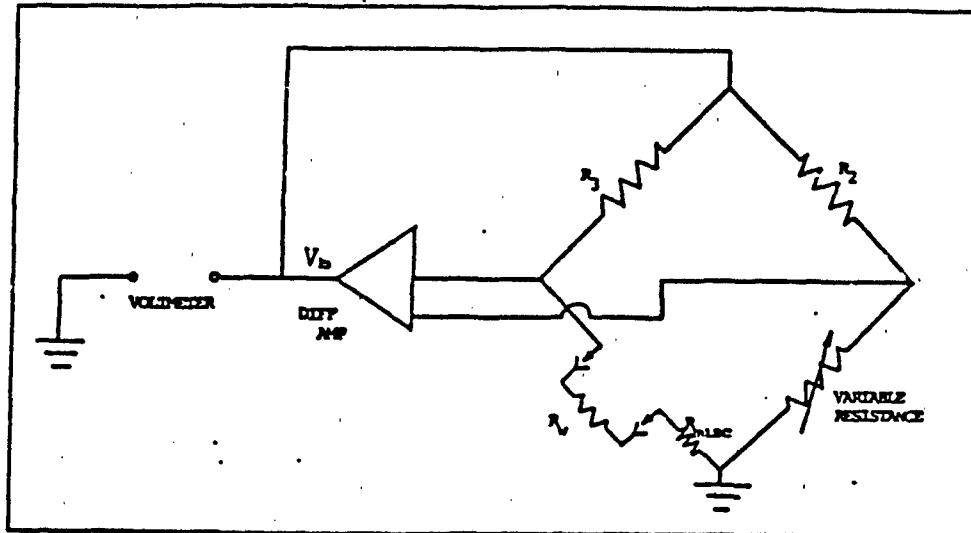
Figure 32. Hot Film Wheatstone Bridge Diagram

control amplifier adjusts the bridge voltage appropriately in order to bring the sensor temperature, and hence its resistance, back to its prescribed value. This "constant temperature" mode of operation is that used for this investigation.

Making the above substitutions into equation (13) and solving for Nusselt number, the equation becomes

$$Nu = V_b^2 \left(\frac{R_v}{(R_u + R_v + R_x + R_{ps} + R_c)^2} \right) \left(\frac{1}{k_f \pi l_s (T_s + T_f)} \right) \qquad (14)$$

where the bridge voltage, V_b, is substituted for the sensor

91

voltage, V_s, and the total resistance of the sensor side of the Wheatstone Bridge is substituted for the sensor resistance alone.

The velocity term that remains buried in the Nusselt number for the time being in equation (14) is actually the "effective" velocity of the fluid with respect to the sensor. Since a given air velocity directed normally over a sensor will transfer heat more efficiently than if directed along its axis, some adjustment must be made to correct for the attitude of the sensor with respect to the flow. Defining an angle, α, as the angle between the axis of the sensor and the fluid velocity vector, the effective velocity can be expressed as

$$V_{eff} = V\sqrt{\sin^2\alpha + k^2\cos^2\alpha} \qquad (15)$$

where the cooling ratio, k, is related to the sensor length to diameter ratio.

Since the air temperature at the sensor surface will be significantly higher than the freestream temperature, some means must be developed to define an average, or "reference", temperature at which the important temperature dependent physical properties of the air can be calculated for use in the above equations. Eckert (8) defined the reference temperature, T_r, as

$$T_r = \frac{1}{2}(T_s + T) + 0.2 \cdot r_c (T_o - T) \tag{16}$$

where T_o is the flow stagnation temperature, and r_c is the adiabatic wall recovery factor. For laminar flows, r_c is equal to the square root of the Prandtl number (15:335). Since the flow over the hot film sensor is always laminar and the Prandtl number for air is approximately 0.71, $r_c = 0.84$.

Using this equation for T_r, the thermophysical properties of air can now be calculated. Density is calculable from the perfect gas law. The value for k_f is given by (15:269)

$$k_f = k_o \left(\frac{T_r}{T_o} \right)^{0.8} \tag{17}$$

where k_o equals 0.242 J/(m·s·K) at $T_o = 273.15$ K. Finally, the viscosity is equal to(15:328)

$$\mu = \mu_o \left(\frac{T_r}{T_o} \right)^{\frac{3}{2}} \left(\frac{T_o + S_1}{T_r + S_1} \right) \tag{18}$$

where $S_1 = 110$ K and $\mu_o = 1.7456 \cdot 10^{-5}$ kg/(m·s) at $T_o = 273.15$ K.

A modification to equation (12), described by Bradshaw (4:115), allows a common Nusselt to Reynolds number

calibration curve to be used for flows of varying temperature. This is achieved by the implementation of a "temperature loading factor", $(T_r/T)^b$, into the three term equation given earlier:

$$Nu\left(\frac{T_r}{T}\right)^b = A + B\sqrt{Re} + CRe.$$ (19)

All the tools required for hot film anemometer calibration are now ready. Before beginning, the temperature/resistance ratio of the film sensor is determined by measuring its resistance at a set of known temperatures. The actual calibration begins with the cooling ratio calibration. The sensor is placed into a known flow at a variety of given angles in order to determine k^2. Finally, the sensor is placed in flows of varying temperature and velocity. The coefficients A, B, C, and b are thus determined.

In the AFIT CTF, The actual calibration process was controlled by a computer code written by Steven DeCook and was based on the calibration processes developed by a series of previous experimenters on the AFIT CTF.

<u>Appendix D.   Hot Film Data Acquisition.</u>

<u>Determination of the Velocity Vector</u>

Figure 33 illustrates the geometry of the hot film
sensor elements with respect to the incoming flow vector.
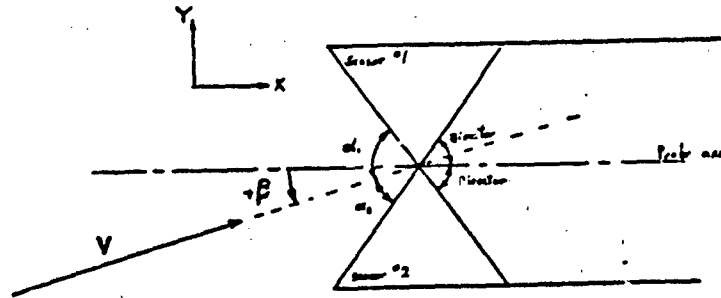
Figure 33.   Hot Film Data Reduction Coordinate System

Using this geometry, the effective velocity seen by each
sensor element is

$$V_{1_{eff}} = V\sqrt{\sin^2\alpha_1 + k_1^2\cos^2\alpha_1} \qquad (20)$$

$$V_{2_{eff}} = V\sqrt{\sin^2\alpha_2 + k_2^2\cos^2\alpha_2} \qquad (21)$$

It is assumed that the bisector, b, of the x-sensor is
known. Combining the above equations and eliminating the
velocity term and one of the angles yields

95

$$\sin^2(2b-\alpha_2) + k_1^2\cos^2(2b-\alpha_2) = \left(\frac{V_{1_{eff}}}{V_{2_{eff}}}\right)^2 (\sin^2\alpha_2 + k_2^2\cos^2\alpha_2) \quad \text{(22)}$$

The only unknown left in the above equation is α_2. This equation can be manipulated via several trigonometric identities and reduced to the form

$$\tan^2\alpha_2\left[\cos^2(2b) + k_1^2\sin^2(2b) - \left(\frac{V_{1_{eff}}}{V_{2_{eff}}}\right)^2\right] + \tan\alpha_2[\sin(4b)(k_1^2-1)]$$

$$+ \left[\sin^2(2b) + k_1^2\cos^2(2b) - k_2^2\left(\frac{V_{1_{eff}}}{V_{2_{eff}}}\right)^2\right] = 0$$

$$\text{(23)}$$

The quadratic formula can now be used to solve for α_2; after which, α_1, β, and V are explicitly calculable. The actual derivation of the above formula is given in the thesis of Decook (5:94-96).

Calculation of Turbulence

The turbulence level is defined by

$$Tu = \frac{\sqrt{(V_x^2 + V_x^2)/2}}{V} \quad \text{(24)}$$

where the root mean square of the above velocity terms is defined by

$$V_{rms} = \bar{V} = \sqrt{\frac{\sum_{i=0}^{N}(V_i - V)^2}{N-1}} \quad \text{(25)}$$

The most direct means of calculating these rms values

96

is by sampling the hot film voltages, converting a series of such samples into a series of x and y velocities, and then substituting these velocities into equation (24). However, this method requires a considerable amount of calculation due to the necessity of calculating all of the individual velocities. An alternate method that was developed by Veesart (17) and expanded on by Decook (5) is to directly transform the rms voltage readings from the two hot film sensors into an estimation of the rms velocity components. These rms velocity components can then be inserted into equation (24) to determine the turbulence level of the airflow.

Beginning with the three term calibration equation given in Appendix C (equation (19))

$$Nu\left(\frac{T_r}{T}\right)^b = A + B\sqrt{Re} + CRe \qquad (26)$$

equation (14) can be substituted for Nusselt number and Re $= \rho V_{eff} d/\mu$. The resulting very large equation can be differentiated to obtain

$$dV_{eff} = \left(\frac{4\left(\frac{Nu\,(T_r/T)^b}{V_b}\right)V_{eff}}{B\sqrt{Re} + 2CRe}\right)dV_b \qquad (27)$$

Using a linear differencing method to approximate the differentials, the above differential relationship can be

97

squared and summed over all of the sampled points to obtain

$$(V_{eff_{rms}})^2 = \left(\frac{4\left(\frac{Nu(T_r/T)^b}{V_b} \right) V_{eff}}{B\sqrt{Re}+2CRe} \right)^2 (V_{b_{rms}})^2 \qquad (28)$$

The above relationship is still in terms of the effective velocities at the sensors. It is necessary to resolve these velocities into the perpendicular velocities via

$$V_p = V_{eff} \left(\frac{\sin\alpha}{\sqrt{\sin^2\alpha + k^2\cos^2\alpha}} \right) \qquad (29)$$

and then transform them into the x and y velocity components with respect to the probe via the transformation

$$V_x = \frac{V_{1_{eff}}+V_{2_{eff}}}{2\cos b} \; ; \quad V_y = \frac{V_{1_{eff}}-V_{2_{eff}}}{2\cos b}. \qquad (30)$$

Differentiating, squaring, and summing these equations over the sample of voltages finally yields

$$\overline{V_x}^2 = \left(\frac{1}{2\cos\alpha} \right)^2 \left((V_{1_{eff_{rms}}})^2 + 2\left(\frac{\sum\limits_{i=1}^{n} dV_{1_{eff}}dV_{2_{eff}}}{n-1} \right) + (V_{2_{eff_{rms}}})^2 \right) \qquad (31)$$

$$\overline{V_y}^2 = \left(\frac{1}{2\sin\alpha} \right)^2 \left((V_{1_{eff_{rms}}})^2 - 2\left(\frac{\sum\limits_{i=1}^{n} dV_{1_{eff}}dV_{2_{eff}}}{n-1} \right) + (V_{2_{eff_{rms}}})^2 \right) \qquad (32)$$

where

$$dV_{1_{eff}} = (V_{1_{eff}})_i - \overline{V}_{1_{eff}} \; ; \quad dV_{2_{eff}} = (V_{2_{eff}})_i - \overline{V}_{2_{eff}} \qquad (33)$$

With the root mean square velocity components thus deter-

98

mined, turbulence can be calculated from equation (24).

Appendix E. Cascade Potential Theory

The derivations of the equations pertaining through potential flow through compressor cascades are simplified by the assumption of constant axial flow through the cascade. Since most linear compressor cascades approximate this behavior quite closely, this is a valid assumption.

Assuming steady and incompressible flow through the cascade, and also assuming that nc losses occur, Bernoulli's equation can be applied both upstream and downstream of the cascade to establish

$$P_1 + \frac{1}{2}\rho V_1^2 = P_2 + \frac{1}{2}\rho V_2^2 \tag{34}$$

where P is the static pressure. From continuity, assuming two dimensional flow

$$V_1 \cos \alpha_1 = V_2 \cos \alpha_2 = V_x \tag{35}$$

where V_x is the constant axial velocity through the cascade.

These two equations can be combined to express the static pressure rise through the cascade in two alternate formats

$$\Delta P = P_2 - P_1 = \frac{1}{2}\rho (V_1^2 - V_2^2) = \frac{1}{2}\rho V_1^2 \left(1 - \frac{\cos^2\alpha_1}{\cos^2\alpha_2}\right) \tag{36}$$

100

This static pressure rise can be non-dimensionalized by dividing through by the inlet dynamic head to create the static pressure rise coefficient

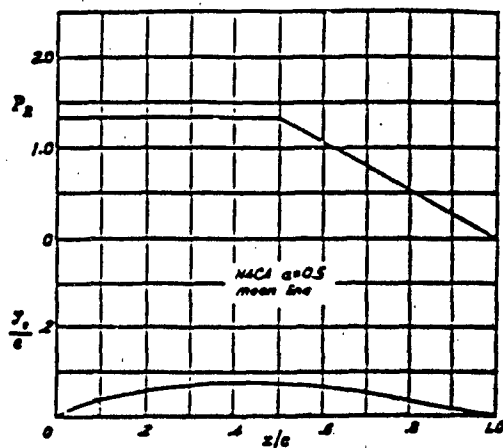$$C_p = \frac{P_2 - P_1}{\frac{1}{2}\rho V_1^2} = 1 - \frac{\cos^2\alpha_1}{\cos^2\alpha_2} \tag{37}$$

Finally, if the total pressure loss coefficient is known, it can be subtracted from the static pressure rise coefficient to get an estimation of the static pressure rise through a cascade with losses, assuming that α_1 and α_2 are constant.

Appendix F. Blade Data

A NACA 64-A905 airfoil with a = 0.5 was used for this study. According to Abbot and Von Doenhoff, the series designator numbers are interpreted as follows. The "6" is the general series designator. The "4" represents the distance from the leading edge of the airfoil, in tenths, of the point of minimum pressure for the symmetric section at zero lift. This also coincides approximately with the point of maximum thickness of the airfoil. The "A" is a modification to the thickness distribution where both the suction and pressure surfaces are essentially straight from the 0.8c point to the trailing edge. The "9" is the design lift coefficient of the camber line, in tenths. The "05" is the maximum thickness of the airfoil in percent of the chord. Finally, "a = 0.5" means that this section is designed to have a uniform aerodynamic load from the leading edge to the 0.5c point.

Table 9 is taken directly from Abbot and Von Doenhoff (1:120-121) and gives the camber line distribution of the airfoil. Finally, Table 10, taken from Veesart (17) represents the surface coordinates of the section, expressed in fractions of chord length, in a coordinate system whose x axis is coincident with the chord line. The origin is at the leading edge of the camber line.

Table 3. NACA a=0.5 Meanline Data

$c_{l_i} = 1.0$	$a_i = 3.04°$	$c_{m_{c/4}} = -0.139$		
x (per cent c)	y_c (per cent c)	dy_c/dx	P_R	$\Delta v/V = P_R/4$
0	0			
0.5	0.345	0.58195		
0.75	0.425	0.53855		
1.25	0.735	0.48360		
2.5	1.295	0.40815		
5.0	2.205	0.33070		
7.5	2.970	0.23365		
10	3.630	0.24890		
15	4.740	0.19690	1.333	0.333
20	5.620	0.15650		
25	6.310	0.12180		
30	6.840	0.09000		
35	7.215	0.05930		
40	7.430	0.02300		
45	7.490	− 0.00630		
50	7.350	− 0.05305		
55	6.965	− 0.09765	1.200	0.300
60	6.405	− 0.12550	1.067	0.267
65	5.725	− 0.14570	0.933	0.233
70	4.955	− 0.16015	0.800	0.200
75	4.130	− 0.16960	0.667	0.167
80	3.265	− 0.17435	0.533	0.133
85	2.395	− 0.17415	0.400	0.100
90	1.535	− 0.16850	0.267	0.067
95	0.720	− 0.15565	0.133	0.033
100	0	− 0.12660	0	0

Table 4. Airfoil Coordinate Point Data

X/Chord	Y/Chord	X/Chord	Y/Chord
1.00000000	0.00000000	0.97986622	0.00183903
ᴜ.93954295	0.00552218	0.89918085	0.00920888
0.84871563	0.01381840	0.79827892	0.01842531
0.71774530	0.02643880	0.63756397	0.03374672
0.55792706	0.03961975	0.47932911	0.04266958
0.40062962	0.04191747	0.35131688	0.04026729
0.30192772	0.03778660	0.25245675	0.03441011
0.20289458	0.03002248	0.15322449	0.02445792
0.10340541	0.01748430	0.08341242	0.01423035
0.06335589	0.01067336	0.04318934	0.00678953
0.02277440	0.00259732	0.01230437	0.00048055
0.00635249	-0.00043930	0.00202666	-0.00074084
0.00000000	0.00000000	-0.00002666	0.00228786
0.00314751	0.00663488	0.00769563	0.01057412
0.01722560	0.01684954	0.03681066	0.02669986
0.05664411	0.03474747	0.07658758	0.04170798
0.09659459	0.04783657	0.14677551	0.06085013
0.19710542	0.07112924	0.24754325	0.07923391
0.29807228	0.08537495	0.34868312	0.08961187
0.39937038	0.09190161	0.48067089	0.09118282
0.56207294	0.08390981	0.64243603	0.07182671
0.72225470	0.05689348	0.80172108	0.04036433
0.85128437	0.03027456	0.90081915	0.02019059
0.94045705	0.01212137	0.98013378	0.00404424
1.00000000	0.00000000		

<u>Vita</u>

Captain James Andrew Rothenflue was born on 15 January, 1965, in Kansas City, Missouri. Upon graduation from Bryan Adams High School in Dallas, Texas, he attended the University of Texas at Arlington where he earned a Bachelor of Science in Aerospace Engineering in 1987. He entered the Air Force under the College Senior Engineering Program, and received his commission from the Air Force Officer Training School in 1987. He was assigned to the Foreign Technology Division at Wright Patterson Air Force Base where he served as an Astronautical Systems Analyst.

Captain Rothenflue enrolled at the Air Force Institute of Technology in 1988 as a part time student. In 1990, he was assigned to AFIT as a full time student in order to complete the masters program in Aeronautical Engineering.

Permanent address: 9905 Shoreview Road
                    Dallas, Texas 75238

1. AGENCY USE ONLY (Leave blank)	2. REPORT DATE December 1991	3. REPORT TYPE AND DATES COVERED Master's Thesis

4. TITLE AND SUBTITLE	5. FUNDING NUMBERS
EXPERIMENTAL INVEESTIGATION INTO THE EFFECTS OF RIBLETS ON COMPRESSOR CASCADE PERFORMANCE	

6. AUTHOR(S)

James A. Rothenflue, Captain, USAF

7. PERFORMING ORGANIZATION NAME(S) AND ADDRESS(ES)	8. PERFORMING ORGANIZATION REPORT NUMBER
	AFIT/GAE/ENY/91D-5

9. SPONSORING/MONITORING AGENCY NAME(S) AND ADDRESS(ES)	10. SPONSORING/MONITORING AGENCY REPORT NUMBER

11. SUPPLEMENTARY NOTES

12a. DISTRIBUTION/AVAILABILITY STATEMENT	12b. DISTRIBUTION CODE
Approved for public release; distribution unlimited	

13. ABSTRACT (Maximum 200 words) The effects of adding riblets to the blades of a subsonic, linear compressor cascade were investigated at the Air Force Institute of Technology. Three blade configurations were tested, including a set of unmodified NACA 64-A905 series blades, a set with riblets applied to the suction surface, and a set with riblets on the pressure surface. Performance was evaluated over a wide range of Reynolds Numbers, and at low and high freestream turbulence levels. Cascade performance was evaluated in terms of total pressure loss coefficient, turning angle, and static pressure rise. No riblet configuration offered robust cascade performance improvements; however, performance was significantly enhanced under certain specific conditions. Riblets also degraded cascade performance at other conditions.

14. SUBJECT TERMS Riblets, linear compressor cascade, total pressure loss coefficient, turning angle, pressure rise			15. NUMBER OF PAGES 118
			16. PRICE CODE

17. SECURITY CLASSIFICATION OF REPORT Unclassified	18. SECUPITY CLASSIFICATION OF THIS PAGE Unclassified	19. SECURITY CLASSIFICATION OF ABSTRACT Unclassified	20. LIMITATION OF ABSTRACT UL

END
FILMED

DATE: 1-92

DTIC